

# Real-Time Discrete Electro-Thermal Model of Dual Active Bridge Converter for Photovoltaic Systems

Yoganandam Vivekanandham Pushpalatha, *Graduate Student Member, IEEE*, Daniel Alexander Philipps, *Graduate Student Member, IEEE*, Timm Felix Baumann, *Graduate Student Member, IEEE*, and Dimosthenis Pefitsis, *Senior Member, IEEE*

**Abstract**—Renewable energy systems have stochastic generation profiles, which affect the performance of the power electronic converters in these systems, especially due to the excessive thermal cycling. In particular, the power semiconductor devices, the most vulnerable components in the power electronic converters, with excessive variation in the junction temperature have reduced lifetime and reliability. Simulating the thermal behaviour of the power devices to study the variations for long periods is not feasible with traditional simulation tools. Consequently, real-time simulations are carried out in such situations. This article presents a real-time discrete electro-thermal model of the dual active bridge converter operating in a photovoltaic system to study the junction temperature variations of the SiC MOSFETs. This model is realized using a low-cost development board with a real-time dual-core microcontroller. This model can subsequently be used to complement the real-time tuning of smart gate drivers to enhance the performance of the SiC MOSFETs. The real-time model is based on experimental data and its performance has been validated using commercially available simulation software.

**Index Terms**—SiC MOSFETs, DSP, dual active bridge converter, extended-phase-shift modulation, photovoltaic systems, real-time model.

## I. INTRODUCTION

The dual active bridge (DAB) converter introduced in [1] is one of the most widely researched DC-DC converters owing to its advantages such as high power density, galvanic isolation, bidirectional power transfer, soft switching capability, buck and boost operation, modular structure, etc. It is suitable for various medium-voltage direct current (MVDC) applications such as battery energy storage systems (BESS), battery charging for electric vehicles, solar photovoltaic (PV) systems, wind power generation, aerospace, etc. [2]–[7]. Earlier DAB converters with silicon-based insulated-gate bipolar transistors (IGBTs) were less efficient. Over time, with advancements in power semiconductor technology, the efficiency of the DAB converters increased gradually [2]. Moreover, recent advances in wide band-gap semiconductors, particularly silicon carbide (SiC) metal-oxide-semiconductor field-effect transistors (MOSFETs) with features such as higher blocking voltage, high-frequency operation, higher temperature conductivity, etc. [8], have improved the efficiency as well as the power density of the DAB converter. In this article, a single-phase DAB converter based on SiC MOSFETs is considered for a grid-connected PV system as shown in Fig. 1, as it can boost the voltage which is required in most of the PV systems [7].

In general, PV systems generate power stochastically and consequently, these systems should be supported by additional

energy storage systems to compensate for imbalances between energy supply and demand. These source variations can cause the junction temperature of the SiC MOSFETs to vary drastically affecting the lifetime and reliability of the MOSFET power modules [9]. Temperature swings cause bond wire lift-off and solder layer delamination accelerating the ageing process of the power modules [10], [11]. Therefore, it is essential to take into account these load and source variations during the design and operation of the DAB converter. Validation of power converters' design and operation is usually performed at the prototyping stage by using software simulation tools, e.g., PLECS or MATLAB/Simulink. Such tools enable easy, fast, and non-destructive validation of various design aspects of power converters, for example, their electrical and thermal performance, as well as control scheme verification. However, running these simulation models requires a considerable amount of time even to evaluate a few milliseconds of the converter's performance. Alternatively, a state-space averaged or a discrete-time model might be used to emulate the DAB converter to analyze its dynamic performance and stability.

A state-space averaged model and a small-signal model of a single-phase DAB converter are presented in [12]. However, the inductor current dynamics and capacitor equivalent series resistance (ESR) are ignored. A generalized averaging method in [13] which uses the 0-th coefficient for the output voltage and 1-st coefficient for the transformer current of the Fourier series to represent the DAB converter requires higher order terms for more accuracy. A full-order discrete-time model averaged over a half-switching period is presented in [14] and a reduced-order discrete-time model for a half-switching period is shown in [15]. A full-time discrete model of the DAB converter with higher accuracy considering the effects of the capacitor ESR has been introduced in [16] and a bilinear approximation method for state transition matrix calculation is presented in [17]. A reduced-order average-value modelling of the DAB converter considering the conduction and core losses is presented in [18]. Even though these models are suitable for assessing the system-level electrical performance of the converter, the performance of power semiconductor devices considering their losses and junction temperature is not considered in the above-mentioned discrete models, which eventually limits the utilization of such models in assessing the DAB converter's thermal behaviour. Introducing thermal models of the converter and power semiconductors will eventually slow down the simulation time further. Moreover, most of the models discussed earlier considered the DAB converter

operating with single-phase-shift (SPS) modulation.

A way to shorten the simulation time of complex simulation models including both electrical and thermal characteristics is to utilize the real-time simulation approach [19], [20]. For system-level simulations of complex multi-converter networks, commercial real-time simulation platforms exist. However, these real-time simulation models do not account for the thermal performance of the power semiconductors. In literature the real-time implementation of converters and power semiconductors in field programmable gate arrays (FPGAs) based on either the datasheet values [21] or experimental results [22] have been shown. However, FPGAs are costly compared to microcontroller units (MCUs) and their need is only limited to conducting real-time simulations of switching transients. A simplified real-time electro-thermal model of the DAB converter employing SiC MOSFET power modules and operating with extended-phase-shift (EPS) modulation has been presented by the authors in [23]. This discrete-time model is implemented using a Texas Instruments (TI) development board with faster simulation time.

The contribution of the present article is on the further extension of the real-time discrete model by including a grid-connected PV system with the DAB converter operating under boost mode and using a maximum power point tracking (MPPT) controller. Moreover, evaluation of the proposed real-time discrete model is performed using commercially available software tools as the benchmark. In addition, the contribution of this paper compared to [23] is the use of experimental thermal characterization of the SiC MOSFET power modules for achieving more accurate thermal modelling, as well as the validation of electrical performance with experimental measurements from a DAB converter laboratory prototype using SiC MOSFET power modules.

The proposed real-time model is suitable for implementation on digital signal processors (DSPs) deployed either locally in gate drivers or as central converter controllers. In particular, this model can be used in the intelligent gate drivers to perform active thermal control [9], [24]–[26] for enhancing either efficiency or reliability of the power electronic converters. The presented real-time model of the DAB converter lowers the simulation time significantly and can be used in digital control design [27], [28]. Furthermore, it can be employed in estimating the remaining lifespan using lifetime models [29].

This article is organized as follows. Section II briefly discusses the system considered (PV generator and DAB converter) and its control structure. In Section III, the discrete-time model of the DAB converter operating with EPS modulation and the discrete-time model of the thermal circuit of a half-bridge leg of the DAB converter are presented. Section IV presents the modelling of the power losses of the SiC MOSFETs in the DAB converter using experimental measurements. In Section V, the realisation of the real-time model using Texas Instruments (TI) development board is presented. Results of the discrete-time model are presented and discussed in Section VI. Section VII concludes this article.

## II. SYSTEM DESCRIPTION, OPERATION AND CONTROL OF DAB CONVERTER FOR GRID-CONNECTED PV SYSTEM

In order to demonstrate the feasibility of the proposed real-time modeling approach, a grid-connected photovoltaic system as shown in Fig. 1 has been considered. This system consists of a PV generator which is interconnected to a low-voltage direct current (LVDC) grid using a single-phase isolated DAB converter. This section presents briefly the components of the system under consideration.

### A. Photovoltaic Generator

The PV generator array of the system is made up of  $N_{\text{mod},p}$  and  $N_{\text{mod},s}$  modules connected in parallel and series respectively. Each of these modules consists of  $N_{\text{cell},s}$  PV cells connected in series. A single PV cell in the module can be modelled as a single diode equivalent circuit as shown in Fig. 2. This model provides a good compromise between simplicity and accuracy [30]. The current-voltage relationship of a single PV module based on this equivalent circuit [31], [32] is given by

$$I_{PV} = I_{ph} - I_o \left( e^{\frac{V_{PV} + I_{PV} R_s}{n_{if} N_{\text{cell},s} V_T}} - 1 \right) - \frac{V_{PV} + I_{PV} R_s}{R_p}. \quad (1)$$

The five unknown parameters: photocurrent  $I_{ph}$ , diode saturation current  $I_o$ , diode ideality factor  $n_{if}$ , series resistance  $R_s$ , and shunt resistance  $R_p$  of the single diode model at standard test conditions (STC): temperature  $T_0 = 298.15$  K ( $25^\circ\text{C}$ ) and solar irradiation  $G_0 = 1$  pu (normalized by  $1 \text{ kW m}^{-2}$ ) can be obtained using the information from the PV module datasheet as given in [33]. Subsequently, these parameters are adjusted to the varying solar irradiation  $G$  and temperature  $T$ . The variable  $V_T$  in (1) is the thermal voltage of the PN junction at STC and is expressed as  $k_B T_0 / q$ , where  $k_B = 1.38 \times 10^{-23} \text{ J K}^{-1}$  is the Boltzmann constant and  $q = 1.602 \times 10^{-19} \text{ C}$  is the electron charge. In this article, (1) is solved by Newton Raphson's iteration method to obtain the  $I - V$  curve [33]. An explicit representation of the above equation based on Lambert W function in the form  $V_{PV} = f(I_{PV})$  [30] or  $I_{PV} = f(V_{PV})$  [34] can also be used to obtain the  $I - V$  curve.

### B. Dual Active Bridge Converter

A single-phase DAB converter [1] comprises two full-bridge circuits and a high-frequency transformer, which provides galvanic isolation between the H-bridge circuits as shown in Fig. 1. The parasitic leakage inductance of the transformer with or without an auxiliary inductor acts as the energy transfer element and the combination of which is represented by the inductor  $L$  ( $= L_{lk} + L_{aux}$ ). The total resistance of the power switches,  $R_{DS(on)}$ , line resistance,  $R_{line}$ , and resistance of the transformer windings,  $R_{windings}$  is represented by the resistor  $R_t = 4R_{DS(on)} + R_{line} + R_{windings}$ . The input capacitor  $C_1$  and output capacitor  $C_2$  in the converter have equivalent series resistances (ESRs)  $R_{C1}$  and  $R_{C2}$  respectively. The primary full-bridge circuit converts the DC voltage  $V_1$  to the square-wave voltage  $v_{AC1}$ . In contrast, the secondary full-bridge circuit converts the square-wave voltage  $v_{AC2}$  to the DC voltage  $V_2$  when power flows in the forward direction (from

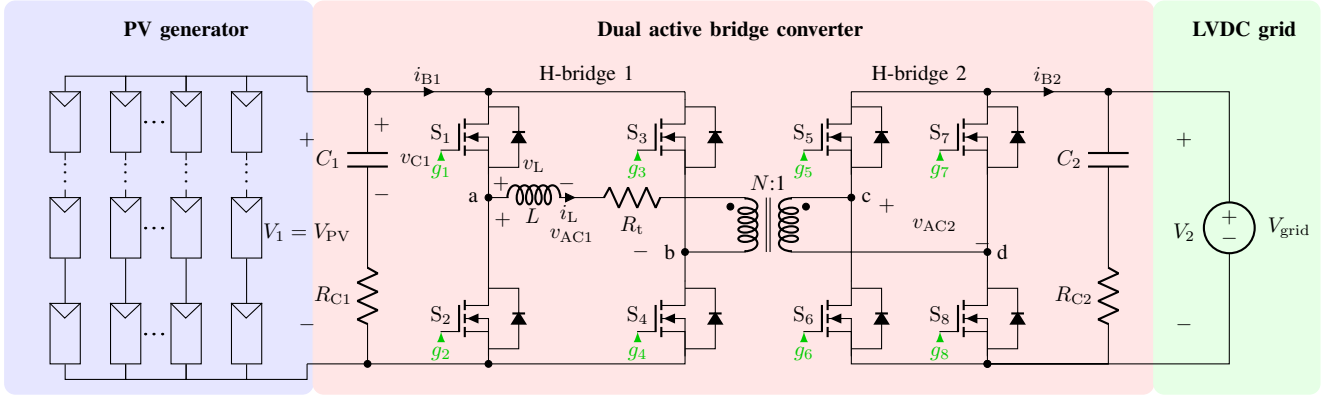


Fig. 1. Photovoltaic system integrated to a LVDC grid through a DAB converter.

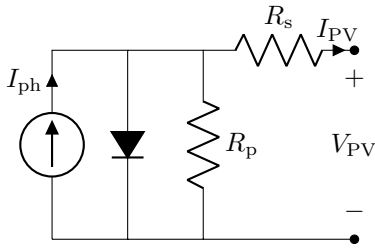


Fig. 2. Equivalent circuit of a single cell in a PV module.

H-bridge 1 to H-bridge 2) and vice versa. The direction and magnitude of power transfer are controlled by the phase shift between the H-bridge voltages  $v_{AC1}$ ,  $v_{AC2}$  which is referred to as single-phase-shift (SPS) modulation. The duty cycle of each of the 8 switches is 50% with a switching frequency of  $f_s$  (switching period  $T_s = 1/f_s$ ). However, high startup current [35], limited soft-switching range, and high circulating inductor current are some disadvantages of this modulation strategy [36]. This circulating inductor current causes power reflow resulting in higher losses in the components than minimum possible. Reflow power refers to the power obtained when the inductor current  $i_L$  and H-bridge 1 voltage  $v_{AC1}$  have different signs. This negative power indicates that a small portion of the power is fed back to the source side.

Consequently, a slightly enhanced modulation referred to as extended-phase-shift (EPS) modulation is introduced to counter this problem in [36]. A zero voltage level is introduced in one of the square-wave H-bridge voltages (usually in the H-bridge with the larger voltage) and it is introduced in the H-bridge 2 voltage  $v_{AC2}$  as shown in Fig. 3. An additional (inner) phase shift  $D_1 T_s/2$  between the half-bridge legs of H-bridge 2 produces the zero voltage level whereas  $D_2 T_s/2$  is the (outer) phase shift between the H-bridges. The duty cycle of the switches remains at 50% as in the case of SPS modulation. The gate signals of the switches ( $g_1, \dots, g_8$ ) indicate the same as shown in Fig. 3. The waveforms of the H-bridge voltages  $v_{AC1}$ ,  $v_{AC2}$ , inductor voltage  $v_L$ , and inductor current  $i_L$  in steady state have half-wave symmetry.

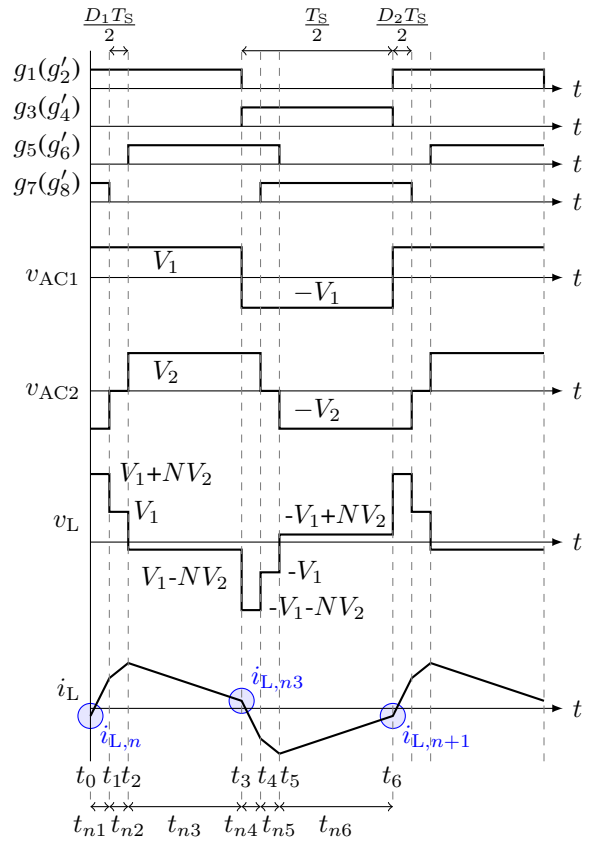


Fig. 3. Steady state waveforms of the DAB converter in EPS modulation.

### C. Maximum Power Point Tracking

The PV system is operated such that it generates maximum power for the present solar irradiation  $G$  and temperature  $T$  by adjusting the voltage  $V_{PV}$  across the PV generator. Among the many available maximum power point tracking (MPPT) algorithms for PV systems, the perturb and observe (P&O) algorithm is still widely used in many industrial applications due to its simplicity [37], [38]. Consequently, this MPPT algorithm is employed in this article and the flow chart of the algorithm is shown in Fig. 4. The sampling frequency of this algorithm is  $T_{MPPT}$ , and the variable  $V_{step}$  is the perturbation

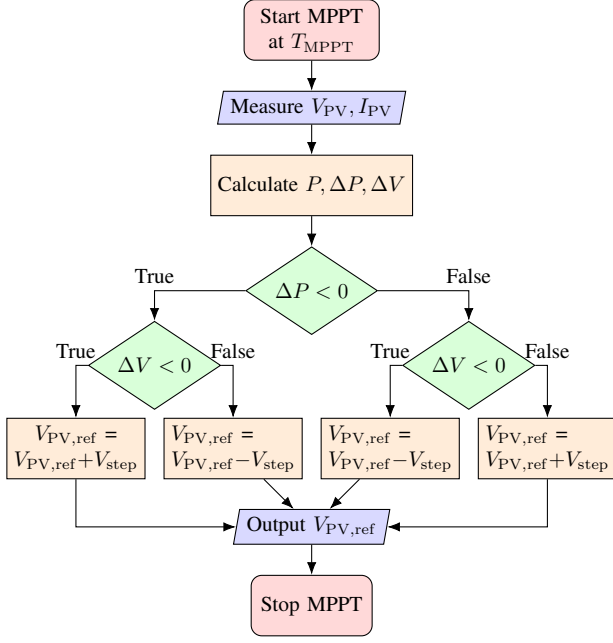


Fig. 4. Flowchart of the P&O MPPT algorithm.

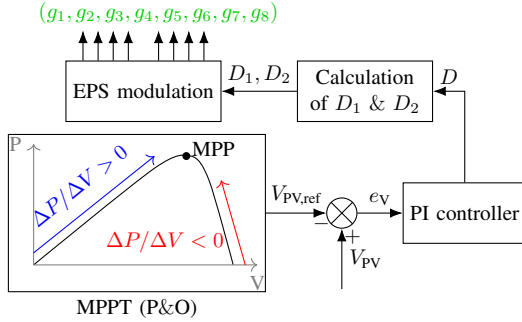


Fig. 5. Block diagram of the voltage control loop of the PV system.

step voltage.

#### D. Voltage Control Loop

The voltage control loop for the PV system is shown in Fig. 5. The MPPT algorithm returns the voltage reference  $V_{PV,ref}$  for the PV generator. Subsequently, a proportional-integral (PI) controller is used to obtain the phase shift  $D$  from the error voltage ( $V_{PV} - V_{PV,ref}$ ) (where the controller frequency  $f_{PI}$  equals  $f_S$ ). This phase shift  $D$  corresponds to the phase shift between the H-bridges for SPS modulation of the DAB converter. This phase shift for SPS modulation is converted to the corresponding phase shifts  $D_1$  and  $D_2$  required for the EPS modulation such that the power reflow is minimum [36]. The inner phase shift factor  $D_1$  is given as

$$D_1 = \begin{cases} \frac{1 + \sqrt{2(1-2D)^2 - 1}}{2} & 0 \leq D < (2 - \sqrt{2})/4 \\ \frac{\sqrt{2(1-2D)}}{2} & (2 - \sqrt{2})/4 \leq D < 1/2 \end{cases}, \quad (2)$$

and the outer phase shift factor  $D_2$  is given as

$$D_2 = \begin{cases} 0 & 0 \leq D < (2 - \sqrt{2})/4 \\ \frac{1 - \sqrt{2(1-2D)}}{2} & (2 - \sqrt{2})/4 \leq D < 1/2. \end{cases} \quad (3)$$

### III. DISCRETE-TIME MODEL

To implement a real-time model of the DAB converter in a PV system, a discrete-time model of the DAB converter (to obtain the electrical performance) and a discrete-time model corresponding to the thermal circuits of the converter (to obtain the thermal performance) are required. They are briefly discussed in the following sub-sections.

#### A. Dual Active Bridge Converter

DAB converter operated with EPS modulation can be represented by the six equivalent circuits corresponding to the six sub-intervals in a single period as shown in Fig. 6. The grid voltage is assumed to be a constant DC voltage and therefore, the dynamics of the output capacitor are not considered. However, if the grid voltage ripple would be considered in the following analysis, an additional state variable would be required. To present the DAB converter in the standard state-space representation, the rate of change of inductor current  $di_L/dt$  and input capacitor voltage  $dv_{C1}/dt$  equations are obtained for each of these circuits. With state vector  $\mathbf{x} = [i_L \ v_{C1}]^T$ , the continuous-time state space representation of a DAB converter during these sub-intervals is given as

$$\dot{\mathbf{x}}(t) = \mathbf{A}_i \mathbf{x}(t) + \mathbf{B}_i \mathbf{u}(t). \quad (4)$$

The state matrices  $\mathbf{A}_i$  and input matrices  $\mathbf{B}_i$  are given as

$$\begin{aligned} \mathbf{A}_1 = \mathbf{A}_2 = \mathbf{A}_3 &= \begin{bmatrix} -(R_t + R_{C1})/L & 1/L \\ -1/C_1 & 0 \end{bmatrix} \\ \mathbf{A}_4 = \mathbf{A}_5 = \mathbf{A}_6 &= \begin{bmatrix} -(R_t + R_{C1})/L & -1/L \\ 1/C_1 & 0 \end{bmatrix} \end{aligned} \quad (5)$$

$$\begin{aligned} \mathbf{B}_1 &= \begin{bmatrix} N/L & R_{C1}/L \\ 0 & 1/C_1 \end{bmatrix} & \mathbf{B}_2 &= \begin{bmatrix} 0 & R_{C1}/L \\ 0 & 1/C_1 \end{bmatrix} \\ \mathbf{B}_3 &= \begin{bmatrix} -N/L & R_{C1}/L \\ 0 & 1/C_1 \end{bmatrix} & \mathbf{B}_4 &= \begin{bmatrix} -N/L & -R_{C1}/L \\ 0 & 1/C_1 \end{bmatrix} \\ \mathbf{B}_5 &= \begin{bmatrix} 0 & -R_{C1}/L \\ 0 & 1/C_1 \end{bmatrix} & \mathbf{B}_6 &= \begin{bmatrix} N/L & -R_{C1}/L \\ 0 & 1/C_1 \end{bmatrix}, \end{aligned} \quad (6)$$

where the subscript  $i$  denotes the sub-interval. The input vector  $\mathbf{u}$  is given as  $[V_{grid} \ I_{PV}]^T$ , where  $V_{grid}$  is the LVDC grid voltage and  $I_{PV}$  is the current from the PV array. The state vector  $\mathbf{x}(t)$  at  $n$ th ( $t = nT_S$ ) and  $(n+1)$ th ( $t = (n+1)T_S$ ) switching cycle are represented as  $\mathbf{x}_n$  and  $\mathbf{x}_{n+1}$  respectively. Table I presents the sub-interval time period, notation, value, and the corresponding state vector representation at the end of each sub-interval for the six sub-intervals.

Sampling the continuous time system at appropriate time instants ( $t_0 = nT_S, \dots, t_6 = (n+1)T_S$ ), the discrete-time model is obtained. The solution for the state vector at the end of each sub-interval is given as

$$\mathbf{x}_{ni} = e^{\mathbf{A}_i t_{ni}} \mathbf{x}_{n(i-1)} + \boldsymbol{\psi}_{ni} \mathbf{u}_n \quad (7)$$

$$\boldsymbol{\psi}_{ni} = \int_0^{t_{ni}} e^{\mathbf{A}_i t_{ni}} \mathbf{B}_i dt = \mathbf{A}_i^{-1} (e^{\mathbf{A}_i t_{ni}} - \mathbf{I}_2) \mathbf{B}_i. \quad (8)$$

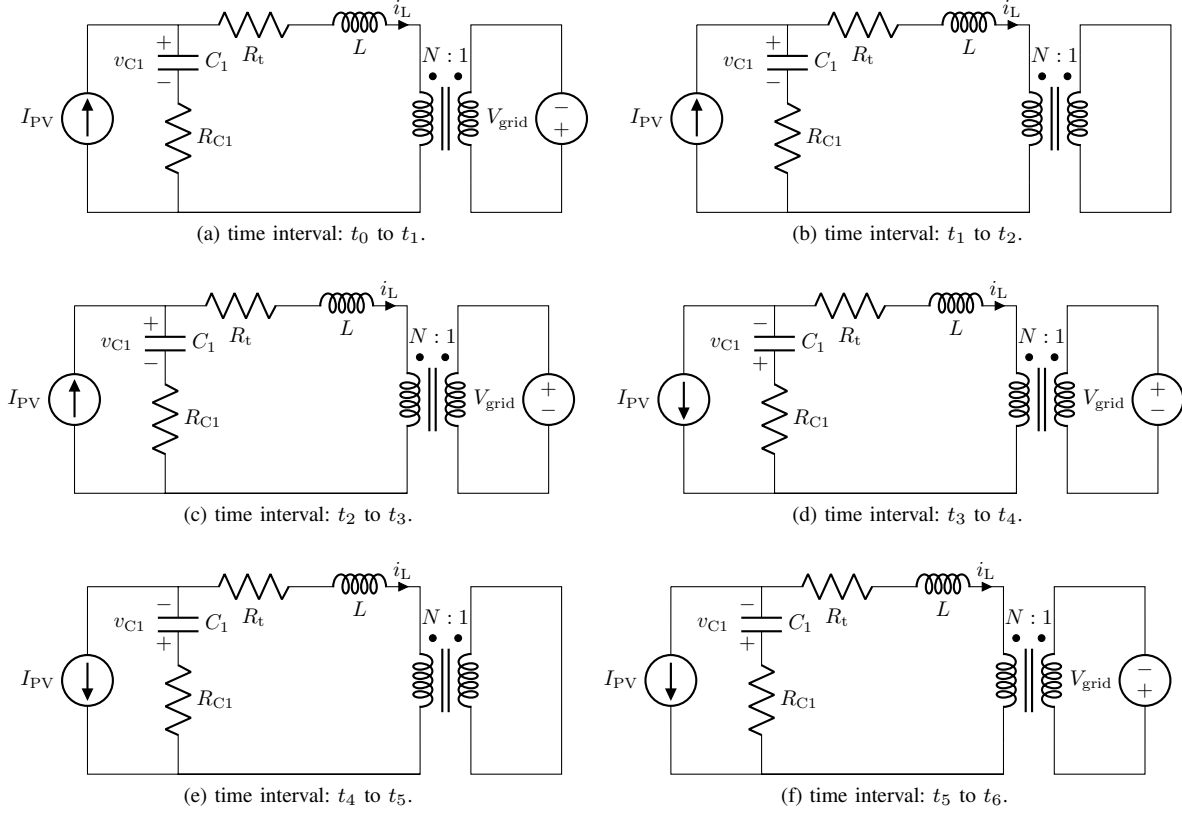


Fig. 6. Equivalent circuits of the DAB converter during different sub-intervals under EPS modulation in a single time period  $T_S$ .

TABLE I  
SUB-INTERVAL PERIODS AND STATE VECTORS IN EPS MODULATION

$i$	Sub-interval period	Notation	Value	State vector at the end of period
1	$(t_1 - t_0)$	$t_{n1}$	$D_2 T_S / 2$	$\mathbf{x}_{n1}$
2	$(t_2 - t_1)$	$t_{n2}$	$D_1 T_S / 2$	$\mathbf{x}_{n2}$
3	$(t_3 - t_2)$	$t_{n3}$	$(1 - D_1 - D_2) T_S / 2$	$\mathbf{x}_{n3}$
4	$(t_4 - t_3)$	$t_{n4}$	$D_2 T_S / 2$	$\mathbf{x}_{n4}$
5	$(t_5 - t_4)$	$t_{n5}$	$D_1 T_S / 2$	$\mathbf{x}_{n5}$
6	$(t_6 - t_5)$	$t_{n6}$	$(1 - D_1 - D_2) T_S / 2$	$\mathbf{x}_{n6} = \mathbf{x}_{n+1}$

From the initial state of the state vector,  $\mathbf{x}_n (= \mathbf{x}_{n0})$  at the  $n$ th switching cycle, the state vector at  $(n + 1)$ th switching cycle can be calculated progressively through the sub-interval state vectors. The complete discrete-time model of the DAB converter for the entire switching time period ( $t_0$  to  $t_6$ ) is

$$\mathbf{x}_{n+1} = \mathbf{F}(D_1, D_2)\mathbf{x}_n + \mathbf{G}(D_1, D_2)\mathbf{u}_n \quad (9)$$

$$\mathbf{F}(D_1, D_2) = e^{\mathbf{A}_6 t_{n6}} e^{\mathbf{A}_5 t_{n5}} e^{\mathbf{A}_4 t_{n4}} e^{\mathbf{A}_3 t_{n3}} e^{\mathbf{A}_2 t_{n2}} e^{\mathbf{A}_1 t_{n1}} \quad (10)$$

$$\begin{aligned} \mathbf{G}(D_1, D_2) = & e^{\mathbf{A}_6 t_{n6}} e^{\mathbf{A}_5 t_{n5}} e^{\mathbf{A}_4 t_{n4}} e^{\mathbf{A}_3 t_{n3}} e^{\mathbf{A}_2 t_{n2}} \boldsymbol{\psi}_{n1} \\ & + e^{\mathbf{A}_6 t_{n6}} e^{\mathbf{A}_5 t_{n5}} e^{\mathbf{A}_4 t_{n4}} e^{\mathbf{A}_3 t_{n3}} \boldsymbol{\psi}_{n2} \\ & + e^{\mathbf{A}_6 t_{n6}} e^{\mathbf{A}_5 t_{n5}} e^{\mathbf{A}_4 t_{n4}} \boldsymbol{\psi}_{n3} \\ & + e^{\mathbf{A}_6 t_{n6}} e^{\mathbf{A}_5 t_{n5}} \boldsymbol{\psi}_{n4} + e^{\mathbf{A}_6 t_{n6}} \boldsymbol{\psi}_{n5} + \boldsymbol{\psi}_{n6}. \end{aligned} \quad (11)$$

The state transition matrices in the above equations can be simplified using fourth-order approximations to reduce the

computation complexity as

$$e^{\mathbf{A}_i t_{ni}} = \mathbf{I}_2 + \mathbf{A}_i t_{ni} + \frac{(\mathbf{A}_i t_{ni})^2}{2!} + \frac{(\mathbf{A}_i t_{ni})^3}{3!} + \frac{(\mathbf{A}_i t_{ni})^4}{4!}, \quad (12)$$

where  $\mathbf{I}_2$  is a  $2 \times 2$  identity matrix. Considering the state-transition matrix  $e^{\mathbf{A}_1 t_{n1}}$  in the first sub-interval  $t_0 - t_1$ , the  $M$ th order truncated Taylor series of this state transition matrix can be given as

$$\mathbf{T}_M(\mathbf{A}_1 t_{n1}) = \sum_{q=0}^M \frac{(\mathbf{A}_1 t_{n1})^q}{q!}, \quad (13)$$

where  $t_{n1} = D_2 T_S / 2$  with  $0 \leq D_2 \leq 1$ . The norm of the absolute truncation error [39], [40] is given as

$$\epsilon_T = \|e^{\mathbf{A}_1 t_{n1}} - \mathbf{T}_M(\mathbf{A}_1 t_{n1})\|. \quad (14)$$

The error values for the first-order truncated series ( $M = 1$ ) to fourth-order truncated series ( $M = 4$ ) for all the  $D_2$  values from 0 to 1 which corresponds to  $t_{n1}$  values from 0 s to 12.5  $\mu$ s are presented in Fig. 7. From this figure, it is clear that the first and second-order truncated series have relatively high errors when compared with the machine epsilon or machine precision value (= macheps). In programming languages such as C, MATLAB, and Python, for a binary32 single precision float data type, the value of macheps is given as  $2^{-23} \approx 1.19e^{-07}$ . In the bottom subplot, the errors for the third and fourth-order truncated series along with machine precision are presented.

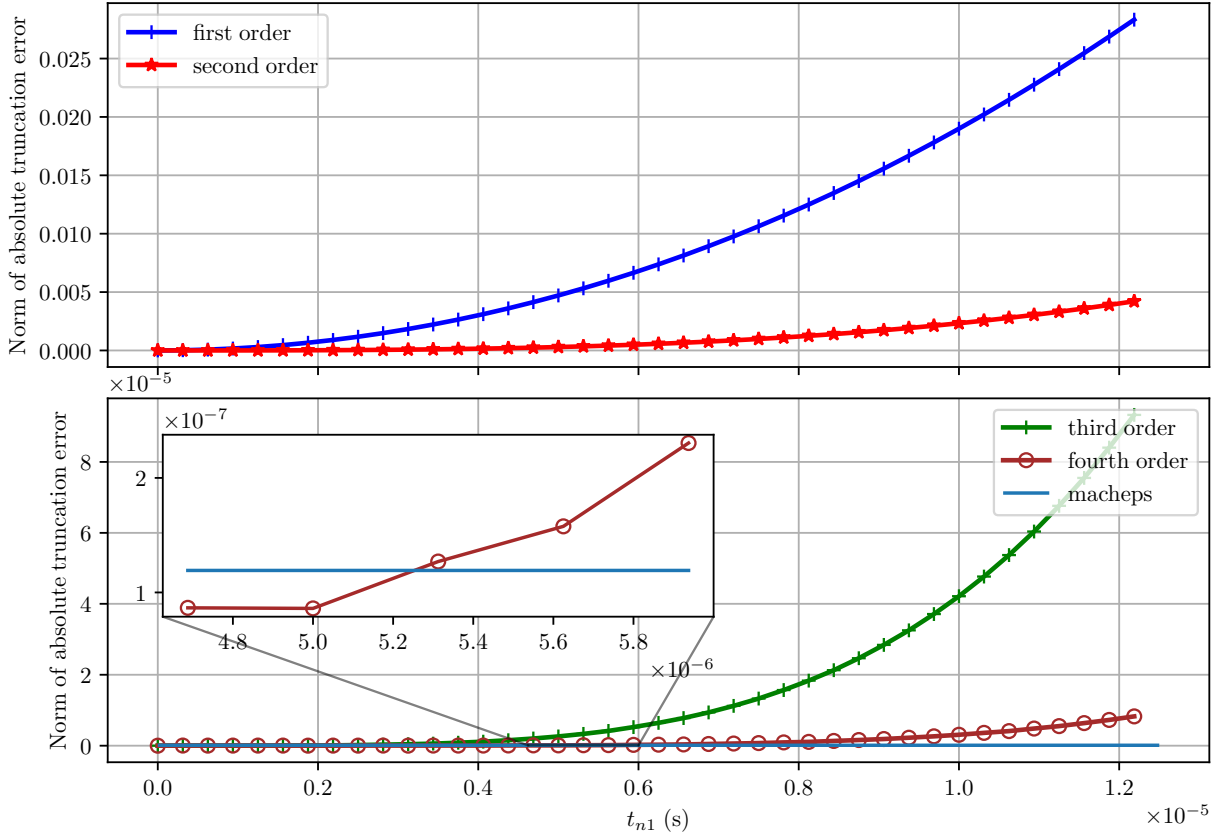


Fig. 7. Norm of the absolute errors of the 1-st, 2-nd, 3-rd, and 4-th order truncated Taylor series of the state transition matrix  $e^{A_1 t_{n1}}$  versus all possible values of  $t_{n1}$  (for  $D_2 = 0$  to  $D_2 = 1$ ).

As observed from this subplot, the errors due to the fourth-order truncated series are lower than the machine precision till  $t_{n1} \approx 5.3 \times 10^{-6}$  s and are relatively close to this value for the higher  $t_{n1}$  values from thereon. Consequently, as a good compromise between accuracy and computational burden, the fourth-order truncated series is selected.

The voltage of the PV array  $V_{PV}$  required in the voltage control loop can be obtained from the state vector  $\mathbf{x}_n$  and input vector  $\mathbf{u}_n$  as

$$V_{PV,n} = [R_{C1} \ 1] \mathbf{x}_n + [0 \ R_{C1}] \mathbf{u}_n. \quad (15)$$

### B. Thermal Circuit of a Half-Bridge Leg in a Dual Active Bridge Converter

In this article, for each half-bridge leg of the DAB converter, a SiC MOSFET half-bridge power module is considered. Each power module is mounted on a separate forced-air cooled heat sink; therefore, an approximate equivalent thermal circuit of a half-bridge leg is considered as shown in Fig. 8. The total power losses (i.e., the sum of the conduction and switching losses) in the switches are represented by the current sources  $P_t, P_b$  for the top and bottom switches in a half-bridge leg respectively, whereas the ambient temperature is represented by the voltage source  $T_{amb}$ . A thermal impedance network for a SiC MOSFET half-bridge module can be obtained either from the manufacturer's datasheet, using finite element method (FEM) analysis software, or through experimental evaluation

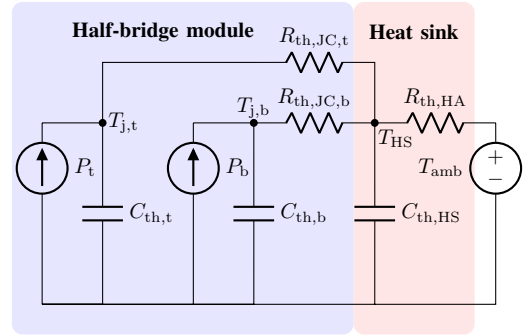


Fig. 8. Equivalent thermal circuit of a half-bridge leg of a DAB converter.

[41]–[43]. The obtained impedance network is usually of a higher order and it can be simplified to a first-order RC network to minimize the computation complexity with a slight compromise in terms of accuracy. Moreover, the thermal impedance networks of the heatsink and insulation material are merged to obtain a simplified first-order RC network.

To obtain the thermal parameters of the SiC MOSFET power module and heatsink, a DC characterization test using a continuous direct current of 100 A has been performed. The chosen test current is expected to generate heat (i.e., power losses) in the same range as in the real-time model of the PV application. The half-bridge module under test is mounted

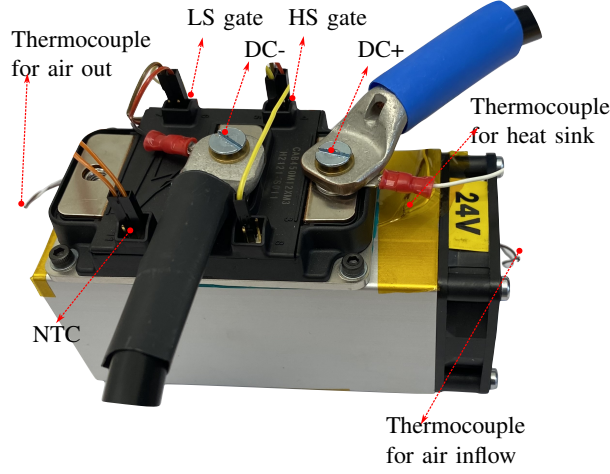


Fig. 9. DC thermal characterization test setup with a CAB450M12XM3 SiC MOSFET power module and heat sink.

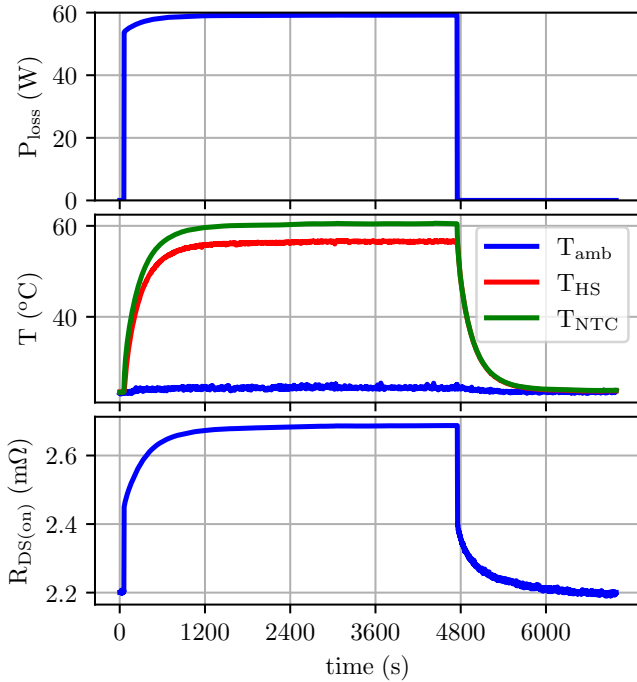


Fig. 10. DC thermal characterization test results: power loss in the module, ambient, heat sink and NTC temperatures and on-state resistance of the high-side switch.

on a heatsink with a phase-change material in between them as shown in Fig. 9. Both upper and lower switching valves of the power modules are kept in the on-state by supplying a positive gate voltage of 15 V. Various temperature sensors (i.e., thermocouples) have been installed as shown in Fig. 9. The results from the DC characterization test are shown in Fig. 10. In this figure, the heat-up and cool-down process under a step response when supplying the test current of 100 A are presented. The top subplot presents the power loss in the module. The second subplot shows the response of three temperatures: the direct bonded copper (DBC) temperature ( $T_{NTC}$ ) measured by the negative temperature coefficient (NTC) thermistor, the heatsink temperature ( $T_{HS}$ ) and the ambient temperature

measured by thermocouples. From this subplot, the thermal capacitance of the entire building block can be extracted, as well as the thermal resistance between the DBC and the heatsink. These parameters can be incorporated into the real-time model, thus improving its accuracy. The bottom subplot of Fig. 10 shows the on-state resistance response (i.e., increase due to the positive temperature coefficient of SiC MOSFETs) of the high-side switch in the half-bridge power module. The thermal resistance can be obtained as

$$R_{th,total} = \frac{T_{NTC,steadystate} - T_{amb}}{P_{loss}} \quad (16)$$

and the thermal capacitance can be obtained as

$$C_{th,total} = \frac{\tau}{R_{th,total}} \quad (17)$$

where  $\tau$  is the time taken by the NTC temperature ( $T_{NTC}$ ) to rise 63.2% of the  $T_{NTC,steadystate}$  from its initial value.

Using the results shown in Fig. 10 and the two equations above, it has been found that the total thermal resistance of the combined power module and heatsink equals  $0.595 \text{ K W}^{-1}$ , and the thermal capacitance is  $343.24 \text{ J K}^{-1}$  respectively. Similarly, the other values required for the thermal network can be obtained from these results.

The continuous-time state-space representation of the thermal network is given as

$$\dot{\mathbf{x}}_{th}(t) = \mathbf{A}_{th}\mathbf{x}_{th}(t) + \mathbf{B}_{th}\mathbf{u}_{th}(t) \quad (18)$$

$$\mathbf{A}_{th} = \begin{bmatrix} M_{eq} & \frac{1}{C_{th,HS}R_{th,JC,t}} & \frac{1}{C_{th,HS}R_{th,JC,b}} \\ \frac{1}{C_{th,t}R_{th,JC,t}} & -\frac{1}{C_{th,t}R_{th,JC,t}} & 0 \\ \frac{1}{C_{th,b}R_{th,JC,b}} & 0 & -\frac{1}{C_{th,b}R_{th,JC,b}} \end{bmatrix} \quad (19)$$

$$M_{eq} = -\frac{R_{th,HA}(R_{th,JC,t} + R_{th,JC,b}) + R_{th,JC,t}R_{th,JC,b}}{C_{th,HS}R_{th,HA}R_{th,JC,t}R_{th,JC,b}} \quad (20)$$

$$\mathbf{B}_{th} = \begin{bmatrix} \frac{1}{C_{th,HS}R_{th,HA}} & 0 & 0 \\ 0 & \frac{1}{C_{th,t}} & 0 \\ 0 & 0 & \frac{1}{C_{th,b}} \end{bmatrix}, \quad (21)$$

where  $\mathbf{x}_{th} = [T_{HS} \ T_{j,t} \ T_{j,b}]^T$  is the state vector of the thermal network ( $T_{HS}$  = heat sink temperature,  $T_{j,t}$  = top switch junction temperature,  $T_{j,b}$  = bottom switch junction temperature) and  $\mathbf{u}_{th} = [T_{amb} \ P_t \ P_b]^T$  is the input vector of the thermal network ( $P_t$  = power losses of the top switch and  $P_b$  = power losses of the bottom switch). In these expressions,  $R_{th,JC,b}$  is the thermal resistance between the junction of the bottom switch and the case of the power module,  $R_{th,JC,t}$  is the thermal resistance between the junction of the top switch and the case of the power module and  $R_{th,HA}$  is the thermal resistance of the heatsink. The corresponding thermal capacitances are shown as  $C_{th,b}$ ,  $C_{th,t}$  and  $C_{th,HS}$ . By sampling the continuous-time system at each switching

TABLE II  
NORM OF ABSOLUTE ERRORS OF TRUNCATED TAYLOR SERIES OF THE  
STATE TRANSITION MATRIX  $e^{\mathbf{A}_{th}T_S}$ .

Truncation order	Norm of absolute error
first	$1.29657 \times 10^{-7}$
second	$9.29247 \times 10^{-9}$

period, the discrete-time model is obtained. The solution for the thermal system (18) is

$$\mathbf{x}_{th,n+1} = e^{\mathbf{A}_{th}T_S} \mathbf{x}_{th,n} + \boldsymbol{\psi}_{th} \mathbf{u}_{th,n} \quad (22)$$

$$\boldsymbol{\psi}_{th} = \int_0^{T_S} e^{\mathbf{A}_{th}T_S} \mathbf{B}_{th} dt \quad (23)$$

$$= \mathbf{A}_{th}^{-1} (e^{\mathbf{A}_{th}T_S} - \mathbf{I}_3) \mathbf{B}_{th} \quad (24)$$

$$e^{\mathbf{A}_{th}T_S} = \mathbf{I}_3 + \mathbf{A}_{th}T_S + \frac{(\mathbf{A}_{th}T_S)^2}{2!}. \quad (25)$$

A second-order approximation of the state transition matrix is used here, where  $\mathbf{I}_3$  is a  $3 \times 3$  identity matrix. Similar to the previous subsection, the error of the truncated Taylor series of the state transition matrix  $e^{\mathbf{A}_{th}T_S}$  of the thermal circuit is calculated. The error values for the first-order and second-order truncated series are shown in Table II. The second-order truncated series is consequently chosen as its error is much lower than the machine precision value.

#### IV. POWER LOSS CALCULATIONS OF THE SiC MOSFETS

The input vector of the discrete-time model of the thermal circuit consists of the power losses of the switches. The total power losses of a MOSFET  $P_{tot}$ , which includes both conduction and switching losses, can be calculated as

$$P_{tot} = P_{cond} + P_{sw} \quad (26)$$

$$P_{cond} = i_{S,RMS}^2 R_{DS(on)}(T_j) \quad (27)$$

$$P_{sw} = (E_{on}(v_{DS}, i_D, T_j) + E_{off}(v_{DS}, i_D, T_j)) f_s, \quad (28)$$

where  $P_{cond}$ ,  $P_{sw}$ ,  $i_{S,RMS}$  are the conduction losses, switching losses, and rms current of a MOSFET respectively. The rms of the current in the MOSFETs needed in the calculation of the conduction losses are calculated from the inductor current values of the discrete-time model of the DAB converter. The rms of the current in the switches  $S_1$  and  $S_2$  are given as

$$\begin{aligned} i_{S1,RMS} = & \frac{1}{6} (6D_1 i_{L,n1}^2 + 6D_1 i_{L,n1} i_{L,n2} - 6D_1 i_{L,n2} i_{L,n3} \\ & - 6D_1 i_{L,n3}^2 + 6D_2 i_{L,n}^2 + 6D_2 i_{L,n} i_{L,n1} \\ & + 6D_2 i_{L,n1}^2 - 6D_2 i_{L,n2}^2 - 6D_2 i_{L,n2} i_{L,n3} \\ & - 6D_2 i_{L,n3}^2 + 6i_{L,n2}^2 + 6i_{L,n2} i_{L,n3} + 6i_{L,n3}^2)^{\frac{1}{2}} \end{aligned} \quad (29)$$

$$\begin{aligned} i_{S2,RMS} = & \frac{1}{6} (6D_1 i_{L,n4}^2 + 6D_1 i_{L,n4} i_{L,n5} - 6D_1 i_{L,n5} i_{L,n6} \\ & - 6D_1 i_{L,n6}^2 + 6D_2 i_{L,n3}^2 + 6D_2 i_{L,n3} i_{L,n4} \\ & + 6D_2 i_{L,n4}^2 - 6D_2 i_{L,n5}^2 - 6D_2 i_{L,n5} i_{L,n6} \\ & - 6D_2 i_{L,n6}^2 + 6i_{L,n5}^2 + 6i_{L,n5} i_{L,n6} + 6i_{L,n6}^2)^{\frac{1}{2}}. \end{aligned} \quad (30)$$

Similarly, the rms of the currents in other switches can be calculated using the subinterval inductor currents. The on-state resistance  $R_{DS(on)}$  of a MOSFET as a function of junction temperature used in conduction losses calculation (27) is given as

$$R_{DS(on)}(T_j) = R_{DS(on),typ} R_{DS(on),nor}(T_j), \quad (31)$$

where  $R_{DS(on),typ}$  is the typical on-state resistance at standard conditions and  $R_{DS(on),nor}(T_j)$  is the normalized on-state resistance  $R_{DS(on)}$  of the MOSFET as a function of junction temperature obtained from the datasheet. Using the damped least squares method, the normalized on-state resistance curve is fit into a polynomial equation and used in the discrete-time model [23].

Double pulse tests (DPTs) were performed to obtain the switching energies of the MOSFETs required in the switching loss calculations (28). The tests were performed for different drain current values ( $i_D$ ) at a drain-to-source voltage of  $v_{DS} = V_{grid}$ , junction temperature  $T_j \approx 25^\circ\text{C}$  and the turn-on and turn-off energy curves  $E_{on,DPT}(i_D)$ ,  $E_{off,DPT}(i_D)$  as a function of drain current  $i_D$  have been obtained. The turn-on and turn-off switching energies as a function of  $v_{DS}$ ,  $i_D$  and  $T_j$  used in switching losses calculation (28) are given as

$$E_{on}(v_{DS}, i_D, T_j) = E_{on,dst}(T_j) \frac{E_{on,DPT}(i_D)}{E_{on,std}} \frac{v_{DS}}{V_{grid}} \quad (32)$$

$$E_{off}(v_{DS}, i_D, T_j) = E_{off,dst}(T_j) \frac{E_{off,DPT}(i_D)}{E_{off,std}} \frac{v_{DS}}{V_{grid}}, \quad (33)$$

where  $E_{on,dst}(T_j)$  and  $E_{off,dst}(T_j)$  are the turn-on and turn-off switching energies as a function of junction temperature at test condition:  $v_{DS,rated}/2$ ,  $i_{D,rated}$  and  $E_{on,std}$ ,  $E_{off,std}$  are the turn-on and turn-off switching energies at test condition:  $v_{DS,rated}/2$ ,  $i_{D,rated}$ ,  $T_j = 25^\circ\text{C}$  that can be obtained from the datasheet. Using the damped least squares method, the turn-on and turn-off energy curves from the DPTs  $E_{on,DPT}(i_D)$ ,  $E_{off,DPT}(i_D)$  and the turn-on and turn-off switching energies as a function of junction temperature  $E_{on,dst}(T_j)$ ,  $E_{off,dst}(T_j)$  are fit into polynomial equations and used in the discrete-time model.

A 1.2 kV 450 A SiC MOSFET half-bridge module CAB450M12XM3 ( $v_{DS,rated} = 1200\text{ V}$ ,  $i_{D,rated} = 450\text{ A}$ ) from Wolfspeed [44] with the gate driver CGD12HBXMP ( $V_{GS,HIGH} = 15\text{ V}$ ,  $V_{GS,LOW} = -4\text{ V}$ ,  $R_G = 1\ \Omega$ ) was used to perform the DPTs. A photo of the experimental setup used to perform the tests is shown in Fig. 11, where an air-cored inductor is used as the load to avoid saturation at elevated testing current values. Exemplary experimental switching waveforms (both turn-off and turn-on) for the drain-to-source voltage  $v_{DS} = 700\text{ V}$  and drain current  $i_D = 250\text{ A}$  are shown in Fig. 12. Using experimental data, the switching energy during turn-on and turn-off for various drain currents at drain-to-source voltage  $v_{DS} = 700\text{ V}$  and their corresponding fitted curves are presented in Fig. 13.

#### V. IMPLEMENTATION OF THE REAL-TIME DISCRETE MODEL

A Texas Instruments (TI) development board LAUNCHXL-F28379D with a 32-bit floating-point microcontroller unit



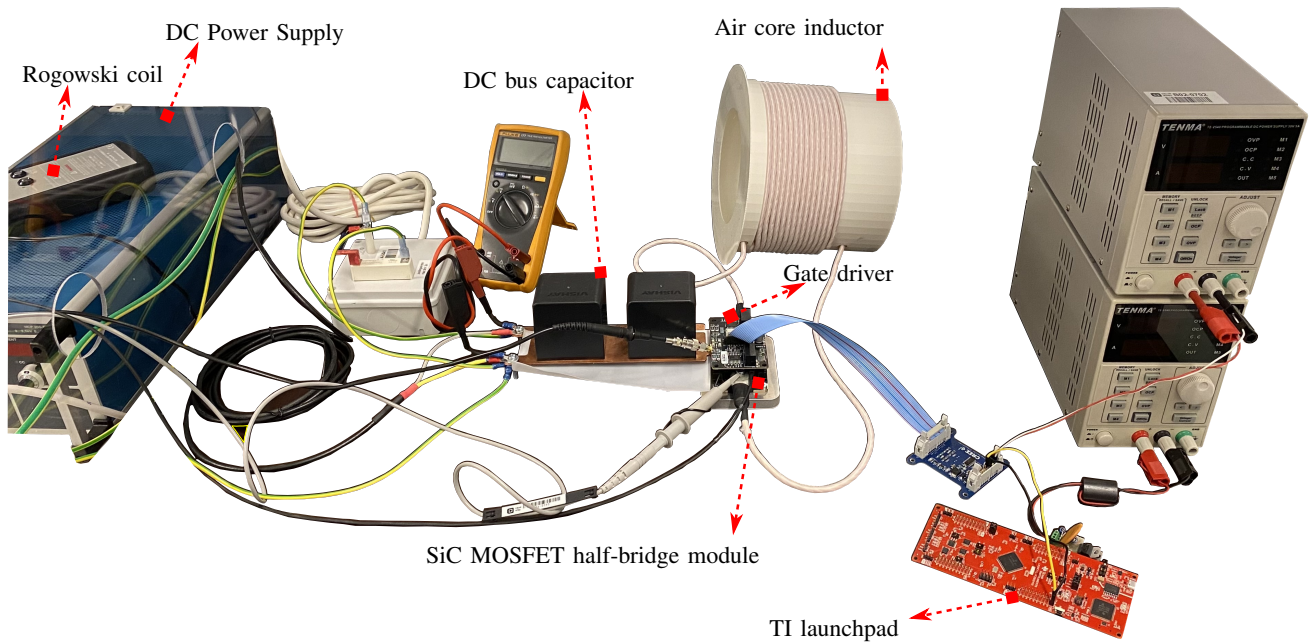
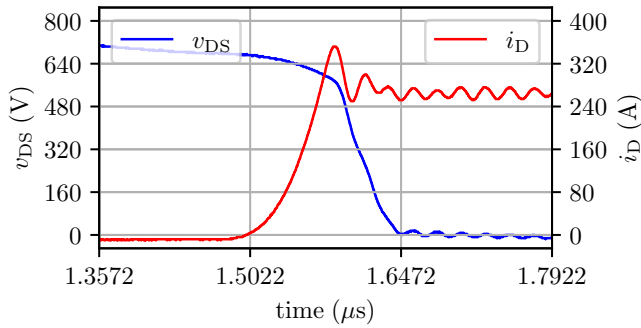
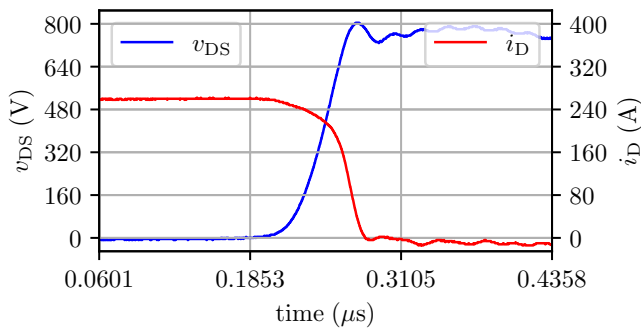


Fig. 11. Double pulse test setup of a 1.2 kV SiC MOSFET half-bridge module (CAB450M12XM3).



(a) Turn-on  $v_{DS}$ ,  $i_D$  waveforms



(b) Turn-off  $v_{DS}$ ,  $i_D$  waveforms

Fig. 12. Experimental switching waveforms of a 1.2 kV SiC MOSFET half-bridge module (CAB450M12XM3) at 700 V and 250 A.

(MCU) with two 32-bit central processing units (CPUs) is used for real-time discrete model realisation (Fig. 14c). The calculations are performed in the interrupt service routines (ISRs) of the enhanced pulse width modulator (ePWM) modules of the MCU. Once every switching period  $T_S$ , ISRs are processed

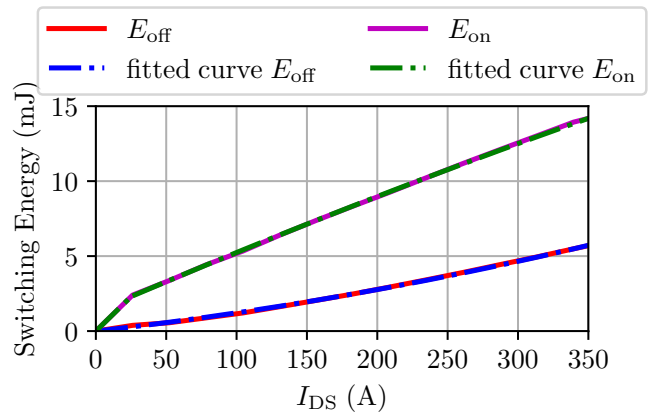
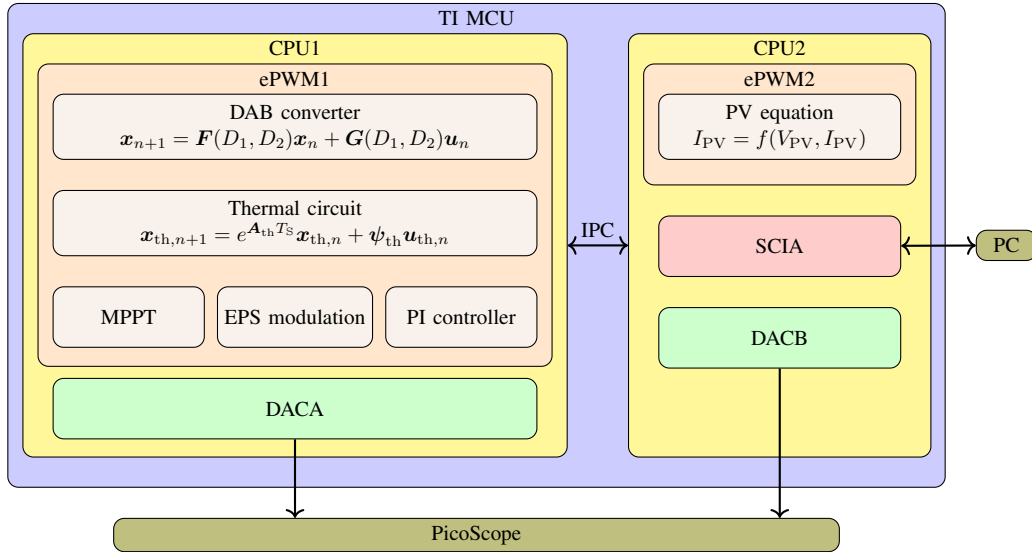
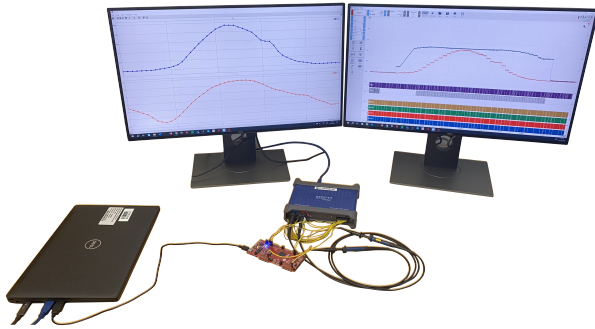


Fig. 13. Energy loss curves of 1.2 kV SiC MOSFET half-bridge module (CAB450M12XM3) at 700 V from the experiments and fitted curves.

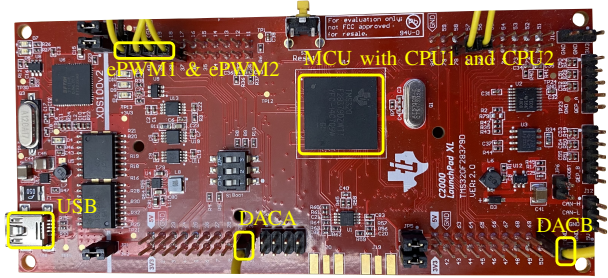
in both the CPUs. In CPU1, the real-time discrete electro-thermal model of the DAB converter, P&O MPPT algorithm, PI controller, and EPS modulation phase shift calculations are computed in the ISR of the ePWM1 module. One of the buffered digital-to-analog converter (DAC) modules DACA in CPU1 is used to visualise the variables through a general-purpose input/output (GPIO) pin. In CPU2, the PV module current-voltage function is solved in the ISR of the ePWM2 module and another buffered DAC module (DACB) is used for data visualisation. The communication between the two CPUs is established using the interprocessor communication (IPC) module. Furthermore, solar irradiation and cell temperature required as inputs to the PV real-time model are obtained from MATLAB/Simulink through a serial communication interface (SCI) module SCIA. A block diagram of the entire implementation is shown in Fig. 14a. This is a way to emulate



(a) Block diagram of the real-time model implementation in TI MCU.



(b) Real-time model implementation setup.



(c) TI development board (LAUNCHXL-F28379D).

Fig. 14. Implementation of the real-time discrete electro-thermal model of the DAB converter.

solar irradiation and cell temperature variations for evaluating the real-time model's validity. However, in a practical system implementation of the real-time discrete model, the PV voltage and current will be measured and fed to the MCU through analogue-to-digital (ADC) modules. The setup used for the real-time discrete model implementation utilising a TI LaunchPad and a PicoScope (3000 series) is shown in Fig. 14b.

The step-by-step process of the real-time model implementation (main program and interrupt service routine) for CPU1 and CPU2 are shown in Figs. 15 and 16 respectively. In CPU1 (Fig. 15), as a first step, the required modules (ePWM1, DACA and IPC) are initialised. Following this, the variables of the DAB converter and thermal network are initialised. After the initialisation process, the main program of the CPU1 waits for the CPU2 to be ready. Once the CPU2 is ready, the ePWM ISRs are enabled and CPU1 goes into an infinite for loop. CPU1 and CPU2 employ the Time-Base submodules in the ePWM modules, which are used to control the frequency of the sawtooth or triangular carrier waveforms used to produce the PWM signals, to synchronise the carrier waveforms from other PWM modules, or provide phase shift between PWM signals, etc. A counter in the Time-Base module counts from zero to a certain value, which depends on the required frequency, and back to zero from that value producing the triangular

waveform required for PWM. When this counter in the Time-Base submodule of the ePWM1 module equals zero, the ISR of the ePWM1 module is processed before returning to the infinite for loop in the main program. In the ISR of the ePWM1, the DACA value is updated with the variable needed for visualisation ( $T_j$ ,  $P_{cond}$ ,  $P_{sw}$ ,  $V_{PV}$ ,  $i_L$ ). After this, the value  $I_{PV}$  of the PV generator computed in CPU2 is updated for use in CPU1. In the next steps, calculations of the discrete-time model of the DAB converter, power losses, and discrete-time model of the thermal network are performed. Finally, the MPPT algorithm is executed to produce the reference voltage, which is utilised in the PI controller calculation to obtain the phase shift value for the SPS modulation. This value is used in the calculation of the phase shifts for EPS modulation using (2) and (3), before acknowledging the interrupt to allow further interrupts and exiting the ISR of the ePWM1.

Similarly, the required modules (ePWM2, DACB, SCIA and IPC) in the CPU2 are initialised first as shown in Fig. 16. After which the variables of the PV generator are initialised and the CPU2 gives a ready signal to CPU1. Once this signal is acknowledged by CPU1, the main program in CPU2 goes into an infinite for loop, where it waits for the new  $G$  and  $T$  values of the PV generator from a personal computer (PC). These values are sent using MATLAB/Simulink through

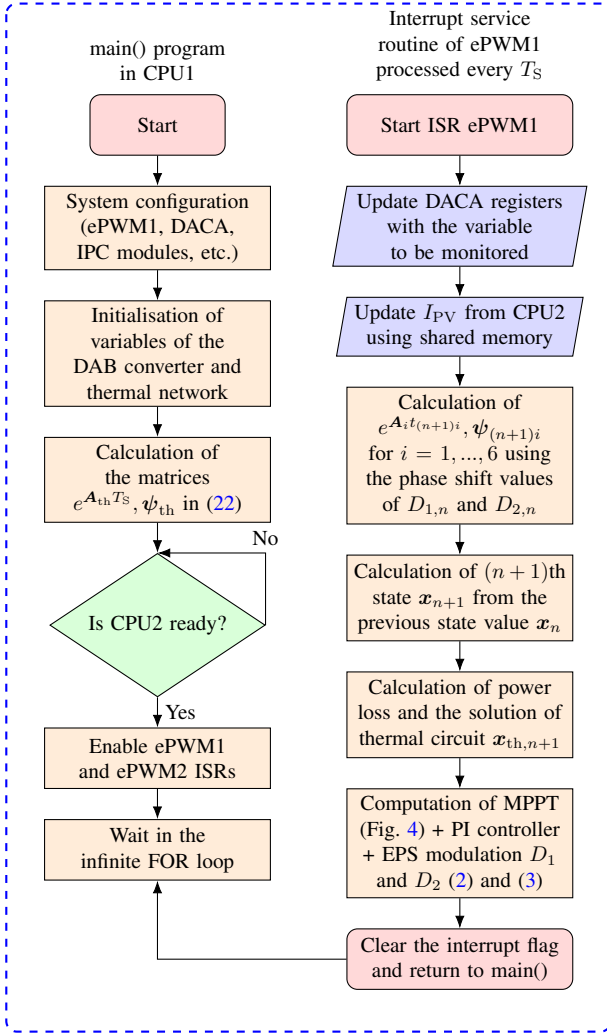


Fig. 15. Flow chart of the programs implemented in CPU1 of the TI MCU.

TABLE III  
PARAMETERS OF THE PV GENERATOR

Parameter	Value
$N_{mod,p}$	14
$N_{mod,s}$	17
$N_{cell,s}$	54
$R_s$	0.284 $\Omega$
$R_p$	157.688 $\Omega$
$I_{ph}$	8.210 A
$I_o$	2.174 nA
$n_{if}$	1.075

serial communication. When the counter in the Time-Base submodule of the ePWM2 module equals zero, the ISR of the ePWM2 module is processed. In the ISR of the ePWM2, the DACB value is updated with the value for visualisation ( $I_{PV}, G, T$ ). After this, the value  $V_{PV}$  of the PV generator computed in CPU1 is updated for use in CPU2. The PV array current-voltage relationship in (1) is solved for  $I_{PV}$  for the present conditions before acknowledging the interrupt and exiting the ISR of the ePWM2.

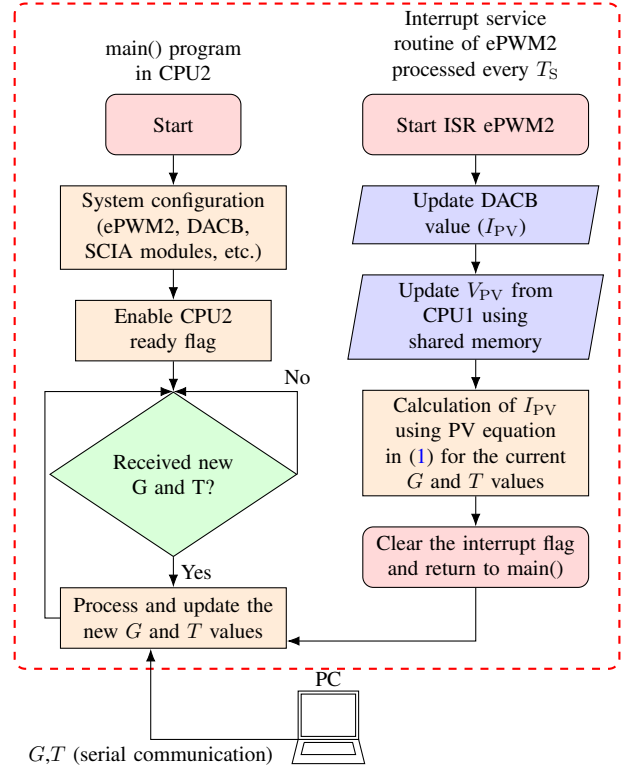


Fig. 16. Flow chart of the programs implemented in CPU2 of the TI MCU.

TABLE IV  
PARAMETERS OF THE DAB CONVERTER

Parameter	Value
$V_{grid}$	700 V
$C_1$	200 $\mu$ F
$L$	18.91 $\mu$ H
$R_{C1}$	1 m $\Omega$
$R_t$	10.4 m $\Omega$
$f_s$	40 kHz
$N$	1

TABLE V  
PARAMETERS OF THE THERMAL CIRCUIT

Parameter	Value
$C_{th,t}$	0.65 J K $^{-1}$
$C_{th,b}$	0.65 J K $^{-1}$
$C_{th,HS}$	20 J K $^{-1}$
$R_{th,Jc,t}$	0.11 K W $^{-1}$
$R_{th,Jc,b}$	0.11 K W $^{-1}$
$R_{th,HA}$	0.175 K W $^{-1}$
$T_{amb}$	25 $^{\circ}$ C

## VI. RESULTS AND DISCUSSION

### A. Results and Analysis

This section presents the results from running the real-time discrete electro-thermal model of the DAB converter and PV generator in the TI MCU. The parameters of the PV generator are given in Table III. The number of series PV modules is chosen such that the voltage across the serialized

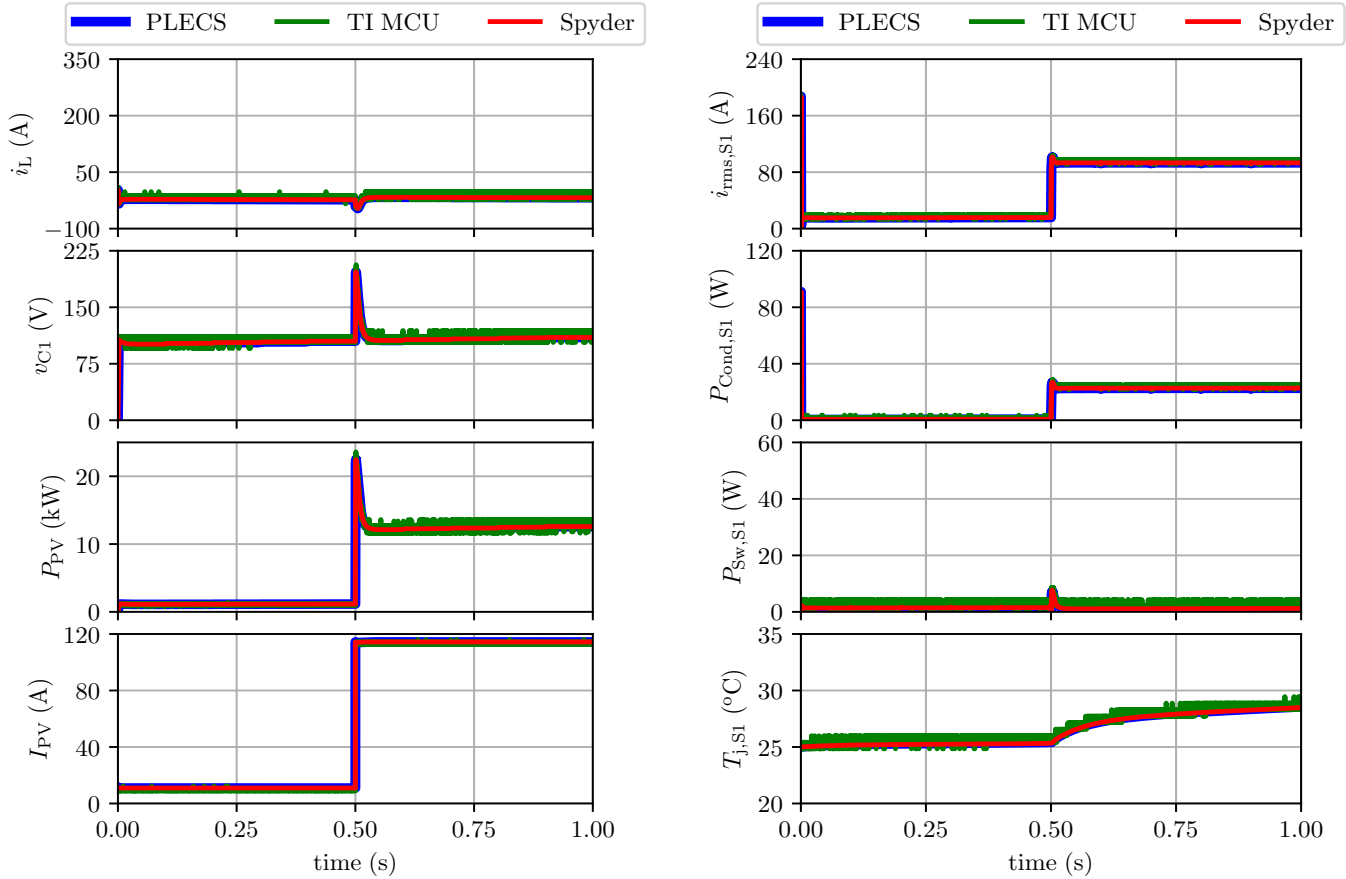
(a) Waveforms of  $i_L$ ,  $v_{C1}$ ,  $P_{PV}$ , and  $I_{PV}$ .(b) Waveforms of  $i_{rms,S1}$ ,  $P_{cond,S1}$ ,  $P_{sw,S1}$ , and  $T_{j,S1}$ .

Fig. 17. Step response waveforms for a step of the solar irradiation from 10% to 100% in PLECS, Spyder, and TI MCU.

TABLE VI  
PLECS SIMULATION SETTINGS

Settings	Value
Solver Type	Variable Step
Solver	auto
Max step size	$1 \times 10^{-6}$
Relative tolerance	$1 \times 10^{-6}$
Refine factor	1

stack is less than the maximum system voltage of 600 V of the selected PV module KC200GT [45]. The number of parallel PV modules is chosen such that the PV generator provides approximately 50 kW of rated power under nominal solar irradiation conditions. The five parameters required for the single-diode equivalent circuit are obtained as given in [45]. The specifications of the DAB converter used in the system are shown in Table IV and the parameters of the thermal circuit are summarized in Table V. The simplified first-order RC network of the SiC MOSFET half-bridge power module (CAB450M12XM3) is obtained using the junction-to-case thermal impedance graph from the datasheet.

To validate the modelling accuracy of the proposed real-time discrete model and compare the simulation results, the

grid-connected PV system, comprising the PV array and DAB converter, has been modelled and simulated using three different tools. The first one is PLECS, which is a commercially available electrical and thermal circuit simulation software. Using the integrated circuit components from the PLECS library, the PV generator and DAB converter were modelled using modelling parameters from the manufacturers' datasheets. The settings used in PLECS are given in Table VI. The second tool is Spyder, an open-source integrated development environment for Python programming language, in which the initial implementation of the discrete-time model has been performed. Finally, the discrete-time model is implemented in the TI MCU to observe the real-time performance.

TABLE VII  
SIMULATION TIME OF DIFFERENT MODELS IN PLECS

PLECS model	Time (s)	
	Variable-step solver	Fixed-step solver
Switching model (thermal and electrical)	15.5004	5.71276
Switching model (only electrical)	4.47017	2.69305
Sub-step events model (only electrical)	24.199	9.36753

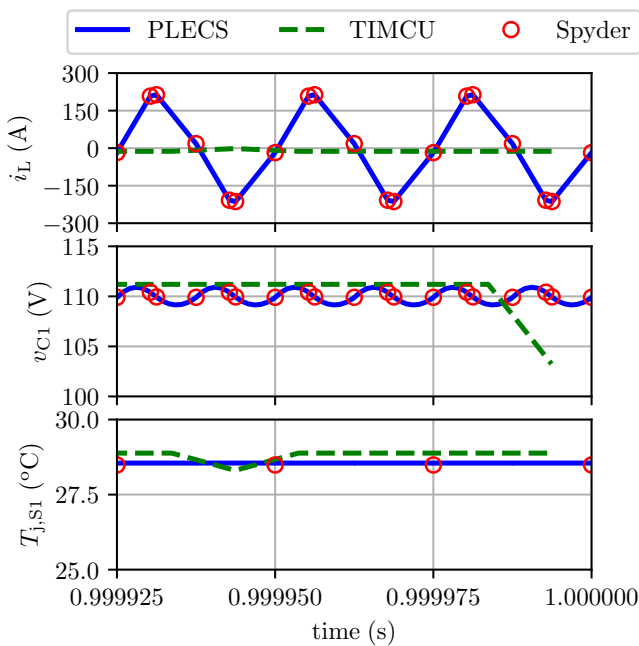


Fig. 18. Waveforms of  $i_L$ ,  $v_{C1}$ ,  $T_{j,S1}$  in the last three cycles of the step response.

Initially, the DAB converter with a constant resistive load was modelled and simulated to evaluate the simulation times for different solver types in PLECS, as well as different simulation tools. The DAB converter in PLECS was modelled in two different ways: the switched model (with and without thermal network) and the sub-step events model. The simulation times of these models for an evaluation period of 1 s are listed in Table VII. The computation time of the sub-step events model presented in [46], [47] is approximately 4-6 times longer compared to the switched model. However, the sub-step events model is intended to be used in a commercial real-time simulator and performs better in such systems. Furthermore, the thermal performance of the DAB converter using the sub-step events model requires additional effort to link this model to the thermal library of PLECS to obtain conduction loss, switching loss and temperature response. In the switched model, placing the heat sink block over the power semiconductor device component computes the losses and temperature without additional effort. Consequently, the switched model with a variable-step solver in PLECS is considered for comparison in the rest of the paper.

The proposed real-time discrete model was then validated under a step change in the solar irradiation from 10% ( $G = 100 \text{ W m}^{-2}$ ) to 100% ( $G = 1000 \text{ W m}^{-2}$ ) with PV generator operating temperature  $T = 25^\circ\text{C}$ . The initial voltage of the PV generator is 0 V, the MPPT frequency  $f_{\text{MPPT}}$  is 10 Hz and the voltage step  $V_{\text{step}}$  is 1 V. These values were chosen to provide satisfactory performance. The MPPT algorithm has a minimum voltage reference set at 100 V and depending upon  $\Delta V$  and  $\Delta P$  the reference voltage  $V_{\text{PV,ref}}$  is either incremented or decremented. In this case, the voltage reference keeps increasing with a step voltage of 1 V. The results of

TABLE VIII  
PERCENTAGE ERROR BETWEEN PLECS AND PROPOSED MODEL

Variables	Percentage error %	
	t = 0.5 s	t = 1 s
$i_{\text{rms},S1}$	-0.15815623	0.02612147
$P_{\text{Cond},S1}$	0.44851761	0.66887556
$P_{\text{Sw},S1}$	-26.90182613	-27.36411679
$T_{j,S1}$	-0.29698567	-0.21977926

the step response in PLECS, Spyder and TI MCU model are shown in Fig. 17. The waveforms of the state variables  $i_L$ ,  $v_{C1}$ , the PV generator power  $P_{\text{PV}}$ , and current  $I_{\text{PV}}$  are shown in Fig. 17a. The waveforms of the rms of the current in the SiC MOSFET  $S_1$ , conduction loss, switching loss, and junction temperature of  $S_1$  are shown in Fig. 17b. These waveforms from PLECS and Spyder are sampled at  $nT_S$  to match with the real-time model results from the TI MCU. Most of the results from PLECS, Spyder and TI MCU match quite well indicating the good performance of the discrete-time model. The error percentage is very low for almost all the quantities in Fig. 17 except for the switching losses, where there is a higher percentage of error as shown in Table VIII. In PLECS, the interpolation of the switching losses is performed for various voltages and temperatures and the interpolation is IP-protected. Moreover, a fitted curve is used for calculating the switching losses in the discrete-time model which results in some error and this error is still low.

Furthermore, the last three cycles of the step response waveforms from PLECS, Spyder and TI MCU as shown in Fig. 18, which also validate the discrete-time model's accuracy. In this figure, the results from the TI MCU are sampled once per switching period and visualised through the TI MCU's DAC GPIO pin. Due to this data conversion, the inductor current,  $i_L$ , that is measured on the DAC GPIO does not contain several data points within the switching period, for example, the peak values of the triangular current shape from PLECS or Spyder. However, internally in the CPUs the real-time calculated  $i_L$  contains a large number of samples which are crucial for estimating the switching and conduction power losses. On the other hand, the input capacitor voltage,  $v_{C1}$  shows a small error between TI MCU, PLECS and Spyder in terms of its DC component, while the ripple in  $v_{C1}$  is not captured in the DAC GPIO for the same reasons as  $i_L$ . Finally, the junction temperature results from the TI MCU are very close to the results using PLECS or Spyder. This is mainly due to the slower dynamics of the junction temperatures compared to the electrical parameters of the converter.

Among others, the most significant advantage of the real-time model is the reduction of the simulation time. On the other hand, the computation time for 1 s step response for the models in PLECS and Spyder are approximately 200 s and 30 s respectively. The computation time of the discrete-time electro-thermal model of the DAB converter, MPPT algorithm, EPS modulation phase-shift calculation, and PI controller in the ISR of the ePWM1 module in CPU1 is approximately 14  $\mu\text{s}$ . Similarly, solving the PV generator equations in the

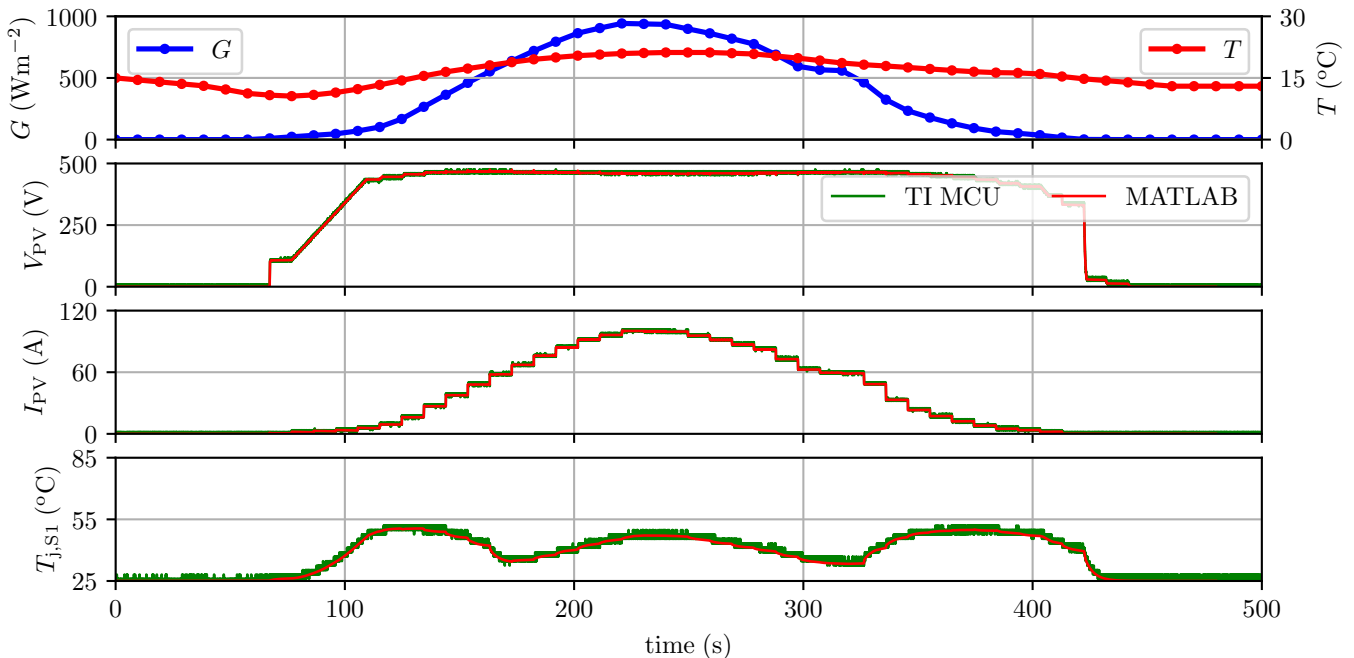


Fig. 19. Waveforms of  $V_{PV}$ ,  $I_{PV}$ ,  $T_{j,S1}$  from TI MCU and MATLAB with solar irradiation and temperature changes.

TABLE IX  
COMPUTATION TIME OF THE MODELS FOR THE STEP RESPONSE

Tool	System	Computation time
PLECS	DAB converter + PV generator	200 s
Spyder	DAB converter + PV generator	30 s
TI MCU (CPU1)	DAB converter	0.56 s
TI MCU (CPU2)	PV generator	0.76 s

ISR of the ePWM2 module in CPU2 using the method in [33] takes approximately  $19\ \mu\text{s}$ . The dual-core of the TI MCU has a clock frequency of 200 MHz which indicates that a single cycle calculation takes about 5 ns. The CPU1 and CPU2 usage are approximately at 56% and 76% respectively with each CPU running ISRs at 40 kHz. The thermal calculations are performed for only one half-bridge in the discrete-time model. If the thermal calculations are extended to the other half-bridge circuits, the CPU1 utilisation rises to 80% approximately. The simulation time results are summarized in Table IX. The timings in this table give a general idea of the performance comparison between the models using the same PC. When operating the DAB converter at higher frequencies, the order of the exponential calculations can be reduced with further optimization of the remaining calculations to reduce the CPU1 utilization. More information on exponential calculation can be found in [40], [48]. Moreover, the thermal calculations need not be carried out in every ISR and, hence, by reducing the frequency of the thermal calculations, the CPU utilization can be further reduced. In addition, CPU2 can be used for other calculations if required and in the case of practical implementation, it can be used entirely for these additional calculations.

The real-time model is used to run longer simulations with variations in solar irradiation and temperature data of a particular location transmitted using MATLAB/Simulink to the TI development board through serial communication. The resulting waveforms from TI MCU are compared with the discrete-time model results implemented in MATLAB (another alternative platform to implement discrete-time model) as shown in Fig. 19. The data is sent with a certain sampling frequency which results in stepped solar irradiation and temperature profile. As a consequence, the PV generator also has this stepped behaviour. This is a way to demonstrate the capabilities of the proposed real-time simulation model. However, the sampling frequency can be increased, thus resulting in a smoother response of the current, which approaches the practical performance of the PV. To demonstrate the variations, the solar irradiation and temperature data for 25 h with one sample per hour is now converted to one input value every 20 s to the TI MCU (Simulink introduces additional interpolated data point every 10 s). The PV generator voltage rises from the initial 0 V to the minimum MPPT reference voltage of 100 V. After this initial value is reached (at around 75 s), the MPPT algorithm increments the PV voltage in steps of 1 V at a frequency of 10 Hz. Consequently, during the start-up phase, the ratio  $\Delta P/\Delta V$  is greater than zero and the PV generator voltage increases to extract the maximum power from the PV generator. Once a certain level of solar irradiation is available, the PV voltage oscillates around 450 V which is closer to the maximum power point (MPP) at STC.

The junction temperature of the SiC MOSFET  $S_1$  at low irradiation levels is comparable to the peak irradiation level due to the circulating inductor current. For the power loss breakdown, the low solar irradiation period shown in Fig. 19

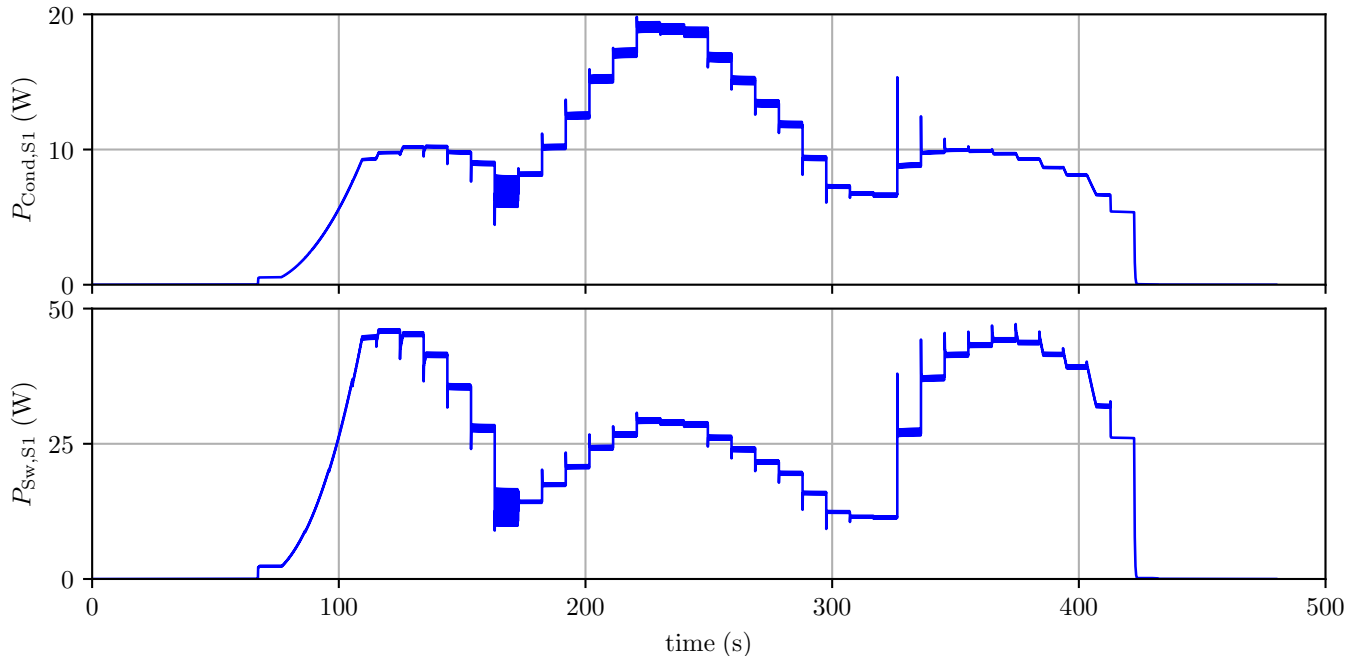


Fig. 20. Waveforms of the conduction loss  $P_{\text{Cond},S_1}$ , switching loss  $P_{\text{Sw},S_1}$  from the discrete-time model implemented in MATLAB.

from 100s to 150s and 325s to 425s has been considered. The corresponding conduction losses and switching losses of the switch  $S_1$  are shown in Fig. 20. It can be observed that the switching losses in these regions are relatively higher than in the other regions. Consequently, the total losses in these regions are higher than in the other regions contributing to higher junction temperature. The MPPT algorithm along with EPS modulation causes these switching losses. Three different scenarios at time = 132.48 s, 181.44 s, 239.616 s are considered and their corresponding  $i_L$ ,  $v_{C1}$ ,  $P_{\text{Cond},S_1}$ ,  $P_{\text{Sw},S_1}$  waveforms given in Fig. 21 clearly shows the loss contribution during these periods. Advanced modulation methods can be modelled in real-time and employed to mitigate the higher losses during low irradiation levels.

A laboratory prototype of the DAB converter has been designed and constructed. For the initial tests, the DAB converter prototype is supplied by a DC power supply and feeds power to a resistive load on the output. The preliminary results of the DAB converter prototype have been used to validate the operation of the discrete-time model in Spyder and the PLECS model. Comparison results for an input DC voltage of  $V_1 = 300$  V at  $f_S = 40$  kHz and with 1 : 1 transformer's turns ratio are shown in Fig. 22. The upper subplot illustrates the inductor current,  $i_L$ , and the bottom subplot shows the voltage across the secondary winding of the transformer,  $v_{AC2}$  (peak voltage of which equals  $V_2$ ) and the direct output voltages  $V_2$  of the DAB converter models in PLECS and Spyder. As observed from this figure, there is a very good match between the experimental and simulation results.

## B. Discussion

This paper proposes a low-cost solution to realize the real-time model of the DAB converter using Texas Instruments (TI) microcontroller units (MCUs) (each MCU costs approximately 10-13\$). It takes advantage of the dual cores in the newly available MCUs from TI. This real-time model poses several advantages ranging from the development and prototyping stage of power converters to converters' online performance enhancement. During the converters' development and prototyping stage, as well as during the verification of their control schemes, the proposed real-time models can be found beneficial in shortening the lead times and minimizing the risk of catastrophic failures. This is still feasible with commercially available real-time simulation platforms, however, the proposed approach in this paper enables the integration of the real-time model with the power converter's MCU or any other digital controller without the need for powerful personal computers. Thus, the proposed real-time models can be integrated with the MCU of the power converter or with the MCU employed on active gate drivers (i.e., in the case of complex modularized converter systems) and enable adaptive control of either the converter as a whole through adaptive modulation schemes or adaptive control of the gate drivers during practical converter's operation. Traditionally, power converters incorporate various sensors for measuring load information (e.g., load current, load voltage etc.) or semiconductor data (e.g., power module temperature etc.) to perform control or safety functions. This information can be well provided to the proposed real-time models that can process it and estimate the converter's electrical or thermal performance. In addition, the real-time models' output signals can command active gate drivers to manipulate the switching

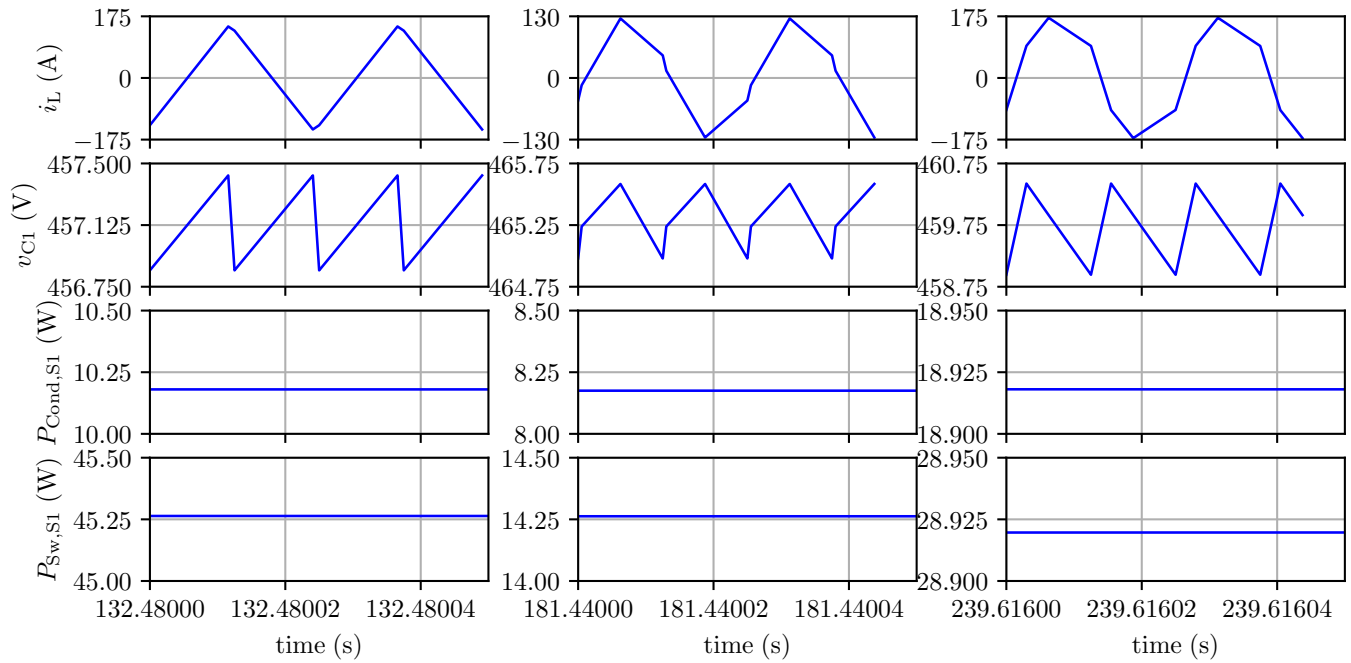


Fig. 21. Waveforms of  $i_L$ ,  $v_{C1}$ ,  $P_{\text{Cond},S1}$ ,  $P_{\text{Sw},S1}$  at three different time periods from the discrete-time model.

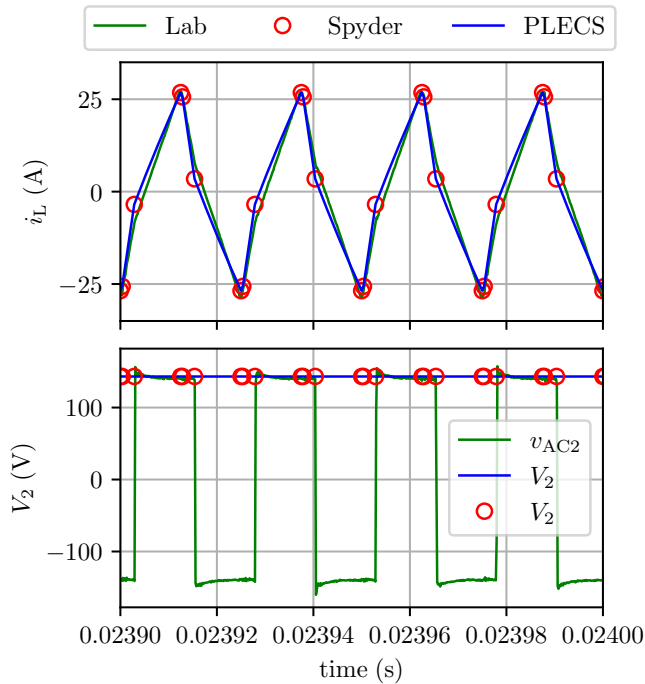


Fig. 22. Comparison of the  $i_L$  and  $V_2$  waveforms from PLECS, Spyder and experimental laboratory measurements of the DAB converter.

behaviour of power semiconductors, and thus continuously minimize switching losses for improving efficiency. The real-time models can also be utilized as a way to estimate the approximate junction temperature and, thus, the expected thermal stress in power semiconductor modules. Such information can be used in a lifetime model to assess the remaining lifetime of

the power module. In this view, the state variables and energy loss can be updated over time to consider the ageing effects of the power modules.

The proposed real-time model is the foundation for developing digital twin models of power converters. To this extent, one can develop the real-time electro-thermal model of a basic building block, for example, the half-bridge SiC MOSFET power module combined with the heatsink that is shown in this paper and develop models of various power converter topologies. An example is the three-phase DAB converter, which exhibits a better performance in terms of losses, efficiency and current stress compared to the single-phase counterpart. Due to the larger number of energy storage components in the three-phase DAB converter (i.e., three inductors and output capacitor), four state variables will be needed and that will result in the use of a  $4 \times 4$  state matrix. The increased model complexity in such a case, will require more computational power from the MCU.

For the proposed real-time model's demonstration, the EPS modulation scheme has been chosen, due to the better power loss performance compared to SPS, especially at low irradiation levels (i.e., low-power operating regions of the converter). However, based on the application operating and performance constraints, other modulation schemes that have been proposed for DABs, such as the triple-phase-shift, can be incorporated in the real-time model.

Increasing the number of parameters that are monitored while the real-time model runs, also increases the MCU's computational requirements. For example, if the junction temperatures of all power semiconductors are to be monitored, the corresponding thermal models must be incorporated into the model, which will increase computational requirements. Even



TABLE X  
INFLUENCE OF  $R_t$  ON THE STATE VARIABLES

State variables	Error
$i_L$ (A)	-0.46122746
$v_{C1}$ (V)	0.00046143

in such cases, due to the limited number of digital-to-analogue (DAC) ports on the MCU (2 in the TI LAUNCHXL-F28379D MCU used), not all junction temperatures can be measured on the oscilloscope. Still, all temperatures can be used internally in the MCU to perform active thermal control or diagnostics.

The model's simplification can also be considered as a way to potentially soften MCU's computational requirements. An example is to neglect parasitic circuit elements, such as the total parasitic resistance  $R_t$ . In this case, the real-time model's accuracy is still acceptable for the capacitor voltage,  $v_{C1}$ , while the inductor current,  $i_L$  value without including  $R_t$  is slightly lower than expected as shown in Table X. This assessment shows the importance of considering the parasitic components in the real-time model, regardless of the slightly increased computational power.

Electrical and thermal characterization of this model is only done once, unless long-time degradation is to be accounted. In the latter case, lifetime models can also be integrated with the real-time model for a multi-dimension evaluation of the power electronic systems. However, the cost for a more complicated real-time model will be the heavier computational and processing power from the MCU or the use of powerful FPGA processors.

## VII. CONCLUSION

This article presents a discrete-time model of a DAB converter interfacing a PV array to the DC grid. This discrete-time model runs in real-time and it has been shown that the electrical and thermal performance of the proposed real-time model of the DAB converter matches the simulation results from a commercially and widely used simulation tool (i.e., PLECS). This is proof of the validity and accuracy of the proposed modelling approach, which can be utilized for simulations to demonstrate the performance of the SiC MOSFETs in the DAB converter during load and source variations. Simulations with the proposed model in Spyder run within 25% of the time a traditional electric circuit simulation tool would use. Consequently, the discrete-time model presented in this paper can be used for prototyping the DAB converters, and their digital control design and the corresponding real-time model can be employed in active gate drivers.

## ACKNOWLEDGMENTS

This work is funded by the Research Council of Norway under the FRIPRO grant 287820 "Adaptive Silicon Carbide Electrical Energy Conversion Technologies for Medium Voltage Direct Current Grids (ASiCC)".

## REFERENCES

- [1] R. De Doncker, D. Divan, and M. Kheraluwala, "A three-phase soft-switched high-power-density DC/DC converter for high-power applications," *IEEE Transactions on Industry Applications*, vol. 27, no. 1, pp. 63–73, Feb. 1991. [Online]. Available: <http://ieeexplore.ieee.org/document/67533/>
- [2] S. Inoue and H. Akagi, "A Bidirectional DC–DC Converter for an Energy Storage System With Galvanic Isolation," *IEEE Transactions on Power Electronics*, vol. 22, no. 6, pp. 2299–2306, Nov. 2007. [Online]. Available: <http://ieeexplore.ieee.org/document/4371545/>
- [3] F. Krismer, "Modeling and Optimization of Bidirectional Dual Active Bridge DC–DC Converter Topologies," Phdthesis, ETH Zurich, 2010. [Online]. Available: [https://www.pes-publications.ee.ethz.ch/uploads/tx\\_etpublications/Krismer\\_2011\\_03\\_17\\_Modeling\\_and\\_Optimization\\_of\\_Bidirectional\\_Dual\\_Active\\_Bridge\\_DC-DC\\_Converter\\_Topologies.pdf](https://www.pes-publications.ee.ethz.ch/uploads/tx_etpublications/Krismer_2011_03_17_Modeling_and_Optimization_of_Bidirectional_Dual_Active_Bridge_DC-DC_Converter_Topologies.pdf)
- [4] R. T. Naayagi, A. J. Forsyth, and R. Shuttleworth, "High-Power Bidirectional DC–DC Converter for Aerospace Applications," *IEEE Transactions on Power Electronics*, vol. 27, no. 11, pp. 4366–4379, Nov. 2012, conference Name: IEEE Transactions on Power Electronics.
- [5] Z. Wang and H. Li, "An Integrated Three-Port Bidirectional DC–DC Converter for PV Application on a DC Distribution System," *IEEE Transactions on Power Electronics*, vol. 28, no. 10, pp. 4612–4624, Oct. 2013. [Online]. Available: <http://ieeexplore.ieee.org/document/6395836/>
- [6] M. Stojadinović, "Bidirectional DC-DC Converters for MVDC Applications," Phdthesis, ETH Zurich, 2020. [Online]. Available: <https://www.research-collection.ethz.ch/handle/20.500.11850/439302>
- [7] E. E. Henaio-Bravo, C. A. Ramos-Paja, A. J. Saavedra-Montes, D. González-Montoya, and J. Sierra-Pérez, "Design Method of Dual Active Bridge Converters for Photovoltaic Systems with High Voltage Gain," *Energies*, vol. 13, no. 7, p. 1711, Jan. 2020, number: 7 Publisher: Multidisciplinary Digital Publishing Institute. [Online]. Available: <https://www.mdpi.com/1996-1073/13/7/1711>
- [8] J. Rabkowski, D. Peftitsis, and H. Nee, "Silicon Carbide Power Transistors: A New Era in Power Electronics Is Initiated," *IEEE Industrial Electronics Magazine*, vol. 6, no. 2, pp. 17–26, Jun. 2012. [Online]. Available: <http://ieeexplore.ieee.org/document/6218284/>
- [9] M. Andresen, K. Ma, G. Buticchi, J. Falck, F. Blaabjerg, and M. Liserre, "Junction Temperature Control for More Reliable Power Electronics," *IEEE Transactions on Power Electronics*, vol. 33, no. 1, pp. 765–776, Jan. 2018, conference Name: IEEE Transactions on Power Electronics.
- [10] J. Lutz, "Packaging and Reliability of Power Modules," in *CIPS 2014; 8th International Conference on Integrated Power Electronics Systems*, Feb. 2014, pp. 1–8.
- [11] S. Pu, F. Yang, B. T. Vankayalapati, and B. Akin, "Aging Mechanisms and Accelerated Lifetime Tests for SiC MOSFETs: An Overview," *IEEE Journal of Emerging and Selected Topics in Power Electronics*, vol. 10, no. 1, pp. 1232–1254, Feb. 2022, conference Name: IEEE Journal of Emerging and Selected Topics in Power Electronics.
- [12] H. Bai, C. Mi, C. Wang, and S. Gargies, "The dynamic model and hybrid phase-shift control of a dual-active-bridge converter," in *2008 34th Annual Conference of IEEE Industrial Electronics*, Nov. 2008, pp. 2840–2845, iSSN: 1553-572X.
- [13] H. Qin and J. W. Kimball, "Generalized Average Modeling of Dual Active Bridge DC–DC Converter," *IEEE Transactions on Power Electronics*, vol. 27, no. 4, pp. 2078–2084, Apr. 2012, conference Name: IEEE Transactions on Power Electronics.
- [14] C. Zhao, S. Round, and J. Kolar, "Full-order averaging modelling of zero-voltage-switching phase-shift bidirectional DC-DC converters," *IET Power Electronics*, vol. 3, no. 3, pp. 400–410, May 2010, conference Name: IET Power Electronics.
- [15] D. Costinett, "Reduced order discrete time modeling of ZVS transition dynamics in the dual active bridge converter," in *2015 IEEE Applied Power Electronics Conference and Exposition (APEC)*, Mar. 2015, pp. 365–370, iSSN: 1048-2334.
- [16] Ling Shi, Wanjun Lei, Jun Huang, Zhuoqiang Li, Yao Cui, and Yue Wang, "Full discrete-time modeling and stability analysis of the digital controlled dual active bridge converter," in *2016 IEEE 8th International Power Electronics and Motion Control Conference (IPEMC-ECCE Asia)*. Hefei, China: IEEE, May 2016, pp. 3813–3817. [Online]. Available: <http://ieeexplore.ieee.org/document/7512904/>
- [17] L. Shi, W. Lei, Z. Li, J. Huang, Y. Cui, and Y. Wang, "Bilinear Discrete-Time Modeling and Stability Analysis of the Digitally Controlled Dual Active Bridge Converter," *IEEE Transactions on Power Electronics*, vol. 32, no. 11, pp. 8787–8799, Nov. 2017, conference Name: IEEE Transactions on Power Electronics.

- [18] K. Zhang, Z. Shan, and J. Jatskevich, "Large- and Small-Signal Average-Value Modeling of Dual-Active-Bridge DC–DC Converter Considering Power Losses," *IEEE Transactions on Power Electronics*, vol. 32, no. 3, pp. 1964–1974, Mar. 2017, conference Name: IEEE Transactions on Power Electronics.
- [19] D. Lena, I. Buraioli, A. Bocca, D. Demarchi, and A. Macii, "An accurate electro-thermal model of sic power mosfets for fast simulations," in *2018 IEEE International Conference on Industrial Technology (ICIT)*, 2018, pp. 623–628.
- [20] H. Cai, U. Raedel, S. Schlegel, and D. Westermann, "Integrated hil simulation of multiple real-time simulator platforms to study the interactions in a multi-converters network," in *2023 IEEE PES Innovative Smart Grid Technologies Europe (ISGT EUROPE)*, 2023, pp. 1–5.
- [21] Z. Shen and V. Dinavahi, "Real-Time Device-Level Transient Electrothermal Model for Modular Multilevel Converter on FPGA," *IEEE Transactions on Power Electronics*, vol. 31, no. 9, pp. 6155–6168, Sep. 2016, conference Name: IEEE Transactions on Power Electronics.
- [22] G. L. Rødal and D. Pefitsis, "Real-time fpga simulation of high-voltage silicon carbide mosfets," *IEEE Transactions on Power Electronics*, vol. 38, no. 3, pp. 3213–3234, 2023.
- [23] Y. V. Pushpalatha, D. Alexander Philipps, and D. Pefitsis, "Real-Time Discrete Model of Dual Active Bridge Converter with Integrated Loss Model of SiC MOSFETs," in *2023 11th International Conference on Power Electronics and ECCE Asia (ICPE 2023 - ECCE Asia)*, May 2023, pp. 2936–2943, iSSN: 2150-6086.
- [24] J. Henn, C. Lüdecke, M. Laumen, S. Beushausen, S. Kalker, C. H. v. d. Broeck, G. Engelmann, and R. W. d. Doncker, "Intelligent Gate Drivers for Future Power Converters," *IEEE Transactions on Power Electronics*, vol. 37, no. 3, pp. 3484–3503, Mar. 2022, conference Name: IEEE Transactions on Power Electronics. [Online]. Available: <https://ieeexplore.ieee.org/document/9537660>
- [25] A. Chanekar, N. Deshmukh, A. Arya, and S. Anand, "Gate Voltage-Based Active Thermal Control of Power Semiconductor Devices," *IEEE Transactions on Power Electronics*, vol. 38, no. 9, pp. 11 531–11 542, Sep. 2023, conference Name: IEEE Transactions on Power Electronics. [Online]. Available: <https://ieeexplore.ieee.org/document/10172032>
- [26] H. B. Ekren, D. A. Philipps, G. Lyng Rodal, and D. Pefitsis, "Four Level Voltage Active Gate Driver for Loss and Slope Control in SiC MOSFETs," in *2022 IEEE 13th International Symposium on Power Electronics for Distributed Generation Systems (PEDG)*. Kiel, Germany: IEEE, Jun. 2022, pp. 1–6. [Online]. Available: <https://ieeexplore.ieee.org/document/9923113/>
- [27] J. Ruthardt, A. Klinkhammer, P. Marx, P. Ziegler, M. Nitzsche, K. Sharma, and J. Roth-Stielow, "Lifetime Extension of Power Semiconductor Devices by Closed-Loop Junction Temperature Control," in *2021 23rd European Conference on Power Electronics and Applications (EPE'21 ECCE Europe)*, Sep. 2021, pp. 1–10.
- [28] J. Shen, J. Zhang, X. Huang, L. Qiu, and Y. Fang, "Active Thermal Management Method for Output-Parallel DAB DC–DC Converters Under Parameter Mismatches and Asymmetrical Modulation," *IEEE Transactions on Power Electronics*, vol. 38, no. 7, pp. 8237–8248, Jul. 2023, conference Name: IEEE Transactions on Power Electronics. [Online]. Available: <https://ieeexplore.ieee.org/document/10098928/citations?tabFilter=papers#citations>
- [29] C. Barbagallo, S. A. Rizzo, G. Scelba, G. Scarcella, and M. Cacciato, "On the Lifetime Estimation of SiC Power MOSFETs for Motor Drive Applications," *Electronics*, vol. 10, no. 3, p. 324, Jan. 2021, number: 3 Publisher: Multidisciplinary Digital Publishing Institute. [Online]. Available: <https://www.mdpi.com/2079-9292/10/3/324>
- [30] E. I. Batzelis, I. A. Routsolias, and S. A. Papanthassiou, "An Explicit PV String Model Based on the Lambert W Function and Simplified MPP Expressions for Operation Under Partial Shading," *IEEE Transactions on Sustainable Energy*, vol. 5, no. 1, pp. 301–312, Jan. 2014, conference Name: IEEE Transactions on Sustainable Energy.
- [31] D. Chan and J. Phang, "Analytical methods for the extraction of solar-cell single- and double-diode model parameters from I-V characteristics," *IEEE Transactions on Electron Devices*, vol. 34, no. 2, pp. 286–293, Feb. 1987, conference Name: IEEE Transactions on Electron Devices.
- [32] D. Sera, R. Teodorescu, and P. Rodriguez, "PV panel model based on datasheet values," in *2007 IEEE International Symposium on Industrial Electronics*, Jun. 2007, pp. 2392–2396, iSSN: 2163-5145.
- [33] L. Callegaro, M. Ciobotaru, and V. G. Agelidis, "Implementation of 3D lookup tables in PLECS for modeling photovoltaic modules," in *2016 Australasian Universities Power Engineering Conference (AUPEC)*, Sep. 2016, pp. 1–6.
- [34] E. I. Batzelis, G. Anagnostou, and B. C. Pal, "A State-Space Representation of Irradiance-Driven Dynamics in Two-Stage Photovoltaic Systems," *IEEE Journal of Photovoltaics*, vol. 8, no. 4, pp. 1119–1124, Jul. 2018, conference Name: IEEE Journal of Photovoltaics.
- [35] X. Fei, Z. Feng, N. PuQi, and W. Xuhui, "Analyzing ZVS Soft Switching Using Single Phase Shift Control Strategy of Dual Active Bridge Isolated DC–DC Converters," in *2018 21st International Conference on Electrical Machines and Systems (ICEMS)*, Oct. 2018, pp. 2378–2381, iSSN: null.
- [36] B. Zhao, Q. Yu, and W. Sun, "Extended-Phase-Shift Control of Isolated Bidirectional DC–DC Converter for Power Distribution in Microgrid," *IEEE Transactions on Power Electronics*, vol. 27, no. 11, pp. 4667–4680, Nov. 2012. [Online]. Available: <http://ieeexplore.ieee.org/document/6111310/>
- [37] T. Esham and P. L. Chapman, "Comparison of Photovoltaic Array Maximum Power Point Tracking Techniques," *IEEE Transactions on Energy Conversion*, vol. 22, no. 2, pp. 439–449, Jun. 2007, conference Name: IEEE Transactions on Energy Conversion.
- [38] J. M. Riquelme-Dominguez and S. Martinez, "Systematic Evaluation of Photovoltaic MPPT Algorithms Using State-Space Models Under Different Dynamic Test Procedures," *IEEE Access*, vol. 10, pp. 45 772–45 783, 2022, conference Name: IEEE Access.
- [39] B. Codenotti and C. Fassino, "Error analysis of two algorithms for the computation of the matrix exponential," *CALCOLO*, vol. 29, no. 1, pp. 1–31, Mar. 1992. [Online]. Available: <https://doi.org/10.1007/BF02576760>
- [40] C. Moler and C. Van Loan, "Nineteen Dubious Ways to Compute the Exponential of a Matrix, Twenty-Five Years Later," *SIAM Review*, vol. 45, no. 1, pp. 3–49, Jan. 2003. [Online]. Available: <http://epubs.siam.org/doi/10.1137/S00361445024180>
- [41] Q. Wang, J. Zhang, F. Iannuzzo, A. S. Bahman, W. Zhang, and F. He, "Improved Temperature Monitoring and Protection Method of Three-Level NPC Application Based on Half-Bridge IGBT Modules," *IEEE Access*, vol. 10, pp. 35 605–35 619, 2022, conference Name: IEEE Access.
- [42] S. Fukunaga and T. Funaki, "Transient thermal network model identification for power module packages," *Nonlinear Theory and Its Applications, IEICE*, vol. 11, no. 2, pp. 157–169, 2020. [Online]. Available: [https://www.jstage.jst.go.jp/article/nolta/11/2/11\\_157/article](https://www.jstage.jst.go.jp/article/nolta/11/2/11_157/article)
- [43] Z. Zhou, J. Yu, X. Ge, J. Duan, C. Luo, and C. Lin, "A Novel Approach of Electrothermal Modeling for Multichip Power Modules," in *2022 IEEE Energy Conversion Congress and Exposition (ECCE)*, Oct. 2022, pp. 1–6, iSSN: 2329-3748.
- [44] Wolfspeed, "1200 V, 450 A All-Silicon Carbide Conduction Optimized, Half-Bridge Module," Datasheet, 2020. [Online]. Available: <https://assets.wolfspeed.com/uploads/2020/12/CAB450M12XM3.pdf>
- [45] Kyocera Solar Inc, "KC200GT Photovoltaic module," Datasheet.
- [46] J. Allmeling and N. Felderer, "Sub-cycle average models with integrated diodes for real-time simulation of power converters," in *2017 IEEE Southern Power Electronics Conference (SPEC)*, 2017, pp. 1–6.
- [47] J. Allmeling, E. Rodriguez-Diaz, and N. Felderer, "Accurate real-time simulation of converters with frequent current commutation using sub-step events," in *2021 IEEE Vehicle Power and Propulsion Conference (VPPC)*, 2021, pp. 1–6.
- [48] D. Bernstein and W. So, "Some explicit formulas for the matrix exponential," *IEEE Transactions on Automatic Control*, vol. 38, no. 8, pp. 1228–1232, Aug. 1993. [Online]. Available: <http://ieeexplore.ieee.org/document/233156/>